2011

Studies of mass loss and outflows from giant stars

Qian Wang
Iowa State University

Studies of mass loss and outflows from giant stars

by

Qian Wang

A dissertation submitted to the graduate faculty

in partial fulfillment of the requirements for the degree of

DOCTOR OF PHILOSOPHY

Major: Astrophysics

Program of Study Committee:

Lee Anne Willson, Major Professor

Walter Anderson

Steven Kawaler

Charles Kerton

Xiaoqing Wu

Iowa State University

Ames, Iowa

2011

DEDICATION

To my parents, for what I become;

To Ling Zhang, for being the light in my life.

TABLE OF CONTENTS

LIST OF TABLES v

LIST OF FIGURES vi

ACKNOWLEDGEMENTS xii

ABSTRACT xiv

CHAPTER 1. From AGB stars to Planetary Nebulae 1

1.1 Overview 1

1.2 The state of AGB stars 2

1.3 Studies on Mass Loss 6

CHAPTER 2. The Bowen code and mass loss 14

2.1 The Bowen code 14

2.1.1 Mass loss rate study 15

2.2 Life cycle of dust in a pulsating atmosphere 16

CHAPTER 3. Multiple spiral arms around AGB stars 19

3.1 Introduction 19

3.2 Modeling methods 20

3.2.1 The Bowen code 20

3.2.2 The properties of the companion 21

3.3 Results 22

3.3.1 The effect of the companion 23

3.3.2 The origin of the spiral arms 24

3.3.3 Spiral arm structure and morphology 29

3.4 Discussion 38
3.4.1 Spiral arm period 38
3.4.2 Observational considerations 46
CHAPTER 4. Conclusions and Future perspectives 52
4.1 Conclusions 52
4.2 Basic equations for AGB atmosphere modeling 53
4.3 Dust formation 55
BIBLIOGRAPHY 58

LIST OF TABLES

Table 1.1 Comparison of Radius, Luminosity, Temperature and surface gravity for the star in Figure 1.1 at different evolutionary phases. 3

Table 2.1 The parameter space used to test mass loss rate. 16

Table 2.2 The stellar parameters used to test the dust life cycle. 16

Table 3.1 The central star parameters 22

Table 3.2 The companion parameters 23

Table 3.3 The properties of shocks between cycle 240 - 300 of Model 5 31

Table 3.4 The average properties of shocks of models 5, 8, 10, 12 31

Table 3.5 The detailed properties of shocks of models 5, 8, 10, 12 35

LIST OF FIGURES

Figure 1.1 Hertzsprung-Russell diagram of a 2 $M_\odot$ evolutionary track from the main sequence to a white dwarf. The values in Table 1.1 are picked from the middle of the shaded regions. The numbers beside the shaded regions indicate the log evolution time scales. The blue track shows a possible born-again evolution triggered by a very late thermal pulse. It has been shifted by $\Delta log T_{eff} \sim -0.2$ and $\Delta log L/L_\odot \sim -0.5$ for clarity. The graph is from Herwig (2005) 3

Figure 1.2 This figure shows the relative abundances of C and O in three different phases during AGB evolution. In Chemical equilibrium, the less abundant elements are completely bound in CO, the excess O (M star) or C (C star) is available for molecule and dust grain formations. This graph is from Höfner (2009) 6

Figure 1.3 The convective regions of $7M_\odot$ between 5th and 6th thermal pulses. The shaded region indicates the convective dominated zones. The dashed lines indicate the hydrogen-helium interface before corresponding dredge-ups. This graph is from Iben (1976) 7

Figure 1.4 This figure shows the pulsation of the atmosphere from the Bowen code. The shaded region has kinetic temperature lower than the radiative equilibrium temperature due to rapid expansion. This provides a region with gas pressure larger than the saturation pressure for dust condensation. Dust may form in this region close to the star. This graph was created by Bowen and appeared in Willson (2000) 8

Figure 1.5 Mass loss rate vs. luminosity for four empirical relations. In the first 3 panels, M= 0.1, 1, 1.4, 2, 2.8 and $4M_{\odot}$. In the fourth panel, M = 5, 6 and $8M_{\odot}$ are added since the equation is suitable for more massive stars. The line cross the curves shows the location of deathline, which is described in Figure 1.7. This graph is from Willson (2000) 10

Figure 1.6 Mass loss rate vs. luminosity for theoretical mass loss relations. The deathline is shown in the middle as in Figure 1.5. This graph is from Willson (2000) 11

Figure 1.7 The evolution of mass and luminosity for solar composition stars experiencing heavy mass loss. There is a sharp "corner" where stars change their evolution phase. This graph is from Willson (2000) 12

Figure 2.1 This figure shows the gas temperature (T_{kin}) and dust temperature (T_{RE}) oscillations vs. time in 4 test zones. 17

Figure 2.2 The top panel shows the normalized carbon density vs. time. The bottom panel is the critical cluster size vs. time. 18

Figure 3.1 Kinetic temperatures in the vicinity of the stronger shocks for Model 5. Contours of kinetic temperatures are superimposed on tracers of computational zones in the models. Zones cluster tightly where shocks appear. Gaps in the zone tracers occur where the model has been rezoned, and dots along the shocks are artifacts of limited sampling in the output file. The contour map is only provided above $2 \times 10^{13} cm$ while the mass motions are traced to deeper levels, hence the artificial boundary of the contour plot. Figure 3.5 shows a more extended region of the same model, Model 5. 24

Figure 3.2 Kinetic temperatures in the vicinity of the weaker shocks for Model 5 as Figure 3.1 and Figure 3.5. Because the planet passes at a different pulsation phase, the shocks are not as strong as in Figure 3.1. 25

Figure 3.3 Molecular acceleration for the same model vs. times as Figure 3.1. The low molecular acceleration between cycles 250 and 251 near $2.5 \times 10^{13} cm$ is due to the destruction of molecules by the rising shock. Additional molecules also show up at the same time below the shock due to extra cooling by expansion. Note the similarity with T_{kin} (Figure 3.1). The periodic pattern in the molecular acceleration between cycles is caused by luminosity variations as the star pulsates. 26

Figure 3.4 Dust acceleration for the same model vs. times as Figure 3.1 and Figure 3.3. Dust appears above 2AU and maintains a periodic pattern as the radiation strength varies. Dust acceleration is more stable than molecular acceleration with time. It provides continuing acceleration from $4 \times 10^{13} cm$ - $8 \times 10^{13} cm$. 27

Figure 3.5 Density variation over a spiral arm period (60 cycles). The stronger shocks show up as higher densities to the left. Note that the density contrast persists beyond $2 \times 10^{14} cm$. 28

Figure 3.6 The same as Figure 3.5 but for a model with artificially low dust and molecular opacity. With less radiative acceleration the large-scale flow is smoother, and near the star, material fails to escape. 29

Figure 3.7 Density vs. time for eleven layers of the model 5. The central layer has radius $R = 1.5 \times 10^{14} cm$ and the separation of the layers is $10^{12} cm$. The density curves are offset by an arbitrary constant C = 0 to 10 from bottom to top. The shock speed can by calculated by tracing the density peaks across the $10^{13} cm$ displayed here. All numbers are listed in Table 3.3. 30

Figure 3.8 Peak density and shock speed vs. cycle number for Model 5. The numbers are listed in Table 3.3. The dotted line gives the density and the solid line, the shock speed computed as illustrated in Figure 3.7. The strong shocks are found before cycle 270 and weaker ones after 270. 32

Figure 3.9 This picture traces the positions of mass shells during cycles 200 - 240 with the density coded by the color. The interval shown in Figure 3.5 occurs in the middle of this plot, with more than two spiral arm periods shown here. The straight line segments trace shock trajectories; they converge towards the heavy line. This convergence produces the spiral arms. 33

Figure 3.10 Density vs. height at cycle 600 for Models 3-6. The companion mass increases with increasing model numbers. There is an artificial offset of C = 1 to 3 for Models 4-6. The front shock is defined as the density drop between position 1 and 2 indicated on Model 5. The rear shock is defined as the density drop between position 3 and 4. The positions of front shocks and rear shocks are chosen to be the same as positions 2 and 4. The density differences are compared between 1 and 2 , 3 and 4 for different cliffs. Similar analyses are done to all cliffs in all models. Numbers are listed in Table 3.5. 34

Figure 3.11 Density vs. height for Model 5 extending to $R = 4.5 \times 10^{16} cm$, showing the spike structure that forms after spiral arms merge. 36

Figure 3.12 Density vs. position in the equatorial plane for Model 5, constructed from the 1D model as described in the text. 37

Figure 3.13 Contour map of the gas kinetic temperature for Model 5. T_{kin} is affected by both the shocks (expansion, compression) and the radiation field. Due to the treatment of non-LTE in the code, T_{kin} does *not* translate easily into intensity of emission. 38

Figure 3.14 Density vs. position in the equatorial plane for Model 1. The dark spiral arms are wide and catch up with each other at around $4 \times 10^{15} cm$. The radial gaps are artifacts of the method we used to construct the map. . 39

Figure 3.15 Density vs. height for Model 1 at cycle 900. The spiral arms in this case merge near $4 \times 10^{15} cm$. The spikes above $6 \times 10^{15} cm$ are not the results of clustered spiral arms. 40

Figure 3.16 Density map for Model 2. The spiral arms are tighter than for model 1 and do not merge inside of $6 \times 10^{15} cm$. 41

Figure 3.17 Density profile of the atmosphere of Model 2 at cycle 900 showing strong density contrast for the spiral arms located at about $3.5 \times 10^{15} cm$, $7 \times 10^{15} cm$ and $10^{16} cm$. 42

Figure 3.18 Spiral density map for Model 7. 43

Figure 3.19 Density profile of the atmosphere of Model 7 at cycle 900. It shows good density contrast for the spiral arms located at about $3 \times 10^{15} cm$, $6 \times 10^{15} cm$ and $8.5 \times 10^{16} cm$. 44

Figure 3.20 Spiral density map for Model 8. While spiral arm stays broad to the edge of the graph, the central region is similar to that of Figure 3.18. . 45

Figure 3.21 Density profile of Model 8 at cycle 900, showing one wide spiral arm near $R = 8 \times 10^{15} cm$. 46

Figure 3.22 Density map for Model 9. We expect the smooth spiral arms where the atmosphere does not lose mass to fast and maintain a steady outflow. . 47

Figure 3.23 Density profile for Model 9 at cycle 900, showing weak contrast in the spiral arms located near $R = 4 \times 10^{15} cm$ and $R = 8 \times 10^{15} cm$. 48

Figure 3.24 Spiral arm period as a function of orbital period from Eqn. 3.3. The vertical dashed lines indicate the periods of Models 1, 5 ,7 and 8. One dotted line is placed at $P_{sa}/P_{puls} = 10$ to show the results with $P_{sa}/P_{puls} > 10$. N is the number of spiral arms for a given spiral arm period. Line N=1 is close to the bottom and intersects with line N = 2 at $P_{sa}/P_{puls} = 3$. 49

Figure 3.25 Companion on a decay orbit. The orbital period is in the vicinity of the Model 5. The decay time scale of the orbital period is 10^4 years. The turn in the shape of spiral is caused by crossing the resonance maximum at $NP_{orb} = MP_{puls}$. This is plotted using a simplified equation based on Eqn. 3.3 not from actual model calculations. 50

Figure 3.26 Column densities in the central plane (thin line), estimated as described in the text, compared with the column density in the unperturbed wind (thick line). Column density alone is not likely to make the spiral arms visible in this example, but they may become visible if the opacity coefficient is higher in the central disk (for example in molecular lines or in the UV). 51

ACKNOWLEDGEMENTS

I would like to take this opportunity to thank Dr. Lee Anne Willson for being a great mentor. With her enthusiasm, her inspiration and her immense knowledge, she has taught me the fun of astronomical researches. For the journey to my Ph.D., I am thankful to have had such a wonderful guide by my side. This thesis would not have been possible without her help. I would also like to thank the committee members of my program of study, Dr. Walter Anderson, Dr. Steven Kawaler, Dr. Charles Kerton, Dr. Xiaoqing Wu. They made valuable suggestions to improve the structure and clarify the concepts in my thesis. I appreciate the support through my Ph.D. study and the writing of my thesis from the Physics and Astronomy Department of Iowa State University and NSF grant AST0708143.

I am indebted to Dr. Curtis Struck, Dr. Massimo Marengo and Dr. Jennifer Sokoloski. Dr. Curtis Struck contributed important insights on the physics of my models. Dr. Marengo provided me the computing facility for the majority part of the studies in this thesis. Without his help, the research would have been much slower. Dr. Sokoloski helped me with the important techniques of scientific writing. Her advice gave me a clear mind when organizing material for my thesis.

I am thankful to Diane Smith, Lori Hockett, Linda Shuck, Gloria Oberender, Deb Schmidt who made my life easier and gave me the best smiles. I am also grateful to all my friends for giving me the other dimensions of my life. I learned about teamworks, competitions, caring and knowing one's limit. These experience together with the scientific knowledge will last a life time.

Through the years of my Ph.D. study, Ling Zhang, my wife, gives me continuous support, encouragement and caring. To her, it is not only expressing my gratitude but also keeping my life long commitment. I also thank my parents, Baoyu Wang and Shurong Wang, without whom I would not be able to enjoy the wonder of life. They raised me, taught me and have

always supported me. I dedicate this thesis to my family.

ABSTRACT

This thesis aims to provide better understanding of mass loss and outflows from asymptotic giant branch stars using the Bowen code. There are 3 projects involved in this thesis. The main project presented here is on the morphology of the outflow when disturbed by a super Jupiter size companion. There exists resonant modes between the pulsation period and orbital period. At different resonant modes, multiple spiral arms with different spiral arm periods form in the outflows. A simple formula gives the spiral arm period as a function of pulsation and orbital periods. Since the resonant modes appear in close orbits, the decay time scale and spiral arm morphology are also presented. These results may explain asymmetry in the outflows that form planetary nebulae. It also explains the origin of the spiral arm structure around some late AGB stars. A 3-D code will ultimately be need to resolve some questions unanswered by the current 1-D models. The paper on the outflow morphology has been submitted to ApJ.

In this thesis, ongoing mass loss studies using the Bowen code are also briefly explained. I generated a large grid of models with varying mass, luminosity, metallicity, mixing length and Bowen model parameters in order to find correlations between the mass loss rate and these parameters. Since dust abundance is an important factor for mass loss, for the third project I tested dust formation in the refrigeration zone which is closer to the photosphere than normal dusty regions. In this test, I assumed that the dust temperature equals to the gas kinetic temperature which is lower than the radiative equilibrium temperature. Since dust temperature is close to the radiative temperature when the dust grain is large, this assumption brings excessive dust into the refrigeration zones. The detailed treatment of dust formation will be refined in future studies.

CHAPTER 1. From AGB stars to Planetary Nebulae

1.1 Overview

Asymptotic Giant Branch (AGB) stars are the final stage in stellar evolution for low and intermediate mass stars. These stars develop very dense cores and vigorous burning shells which greatly increase the size of the stars. Therefore the surface gravity is very low compared to their main sequence counterparts. As the core grows bigger, a series of thermonuclear flashes occur. The flashes change the size of the star temporarily and cause the deepening of the convective zones to bring up the heavy elements, so the abundance of the surface elements changes as well. At the same time, due to the instability in the H and He ionization regions, the stellar atmosphere starts to pulsate at a period on the order of 1 year. Energy is transferred into the atmosphere by shocks generated through pulsation. This results in the levitation of gaseous materials to cooler regions up in the atmosphere. When gas is significantly cooled down, molecules and dust grain are formed. Dust grains are very efficient in absorbing radiations and transferring momentum into the gas. This further pushes the material out of the gravitational trap of the star and forms a mass-losing outflow. When the mass loss rate is low, it does not change the evolution of the star significantly and the luminosity and the radius of the star keep increasing. This in turn stimulates the mass loss rate. Eventually the moderate mass outflow becomes a "superwind" (Bowen & Willson, 1991) that terminates the stellar evolution.

After the envelope is removed, the surface temperature increases dramatically to above 10000K. The blue light from the central star ionizes the escaping envelope and turns the latter into a spectacular planetary nebula. Planetary nebulae, unlike their spherically symmetric progenitors, always appear in a wide variety of shapes. Therefore the morphology of the planetary nebulae is of great interest to astronomers. Magnetic fields, close companions and

central disks are often thought to be the origin of this asymmetry.

The above is a short story of this transition stage between AGB stars and white dwarfs. Most of my studies focused on the mass loss of this stage. Since mass loss phase is only part of the AGB evolution, most of the modeling are based on late AGB stars. The questions I am trying to answer are: Why do stars lose mass after choosing not to for a billion years? What mechanisms dominate the mass loss process? How much can a small companion contribute to the planetary nebula morphology? Chapter 1 is a general overview of the properties of AGB stars, which set stages for this mass outflow. In Chapter 2, I talk about studies of mass loss and grain formation. Our mass loss formula covers a large parameter space and is intended to find the intrinsic dependence of mass loss on the stellar parameters and physical processes. In Chapter 3, morphology of the outflow when disturbed by a small companion is presented. We find interesting multiple spiral arms patterns caused by the resonance between the pulsation period and orbital period. Chapter 4 presents a new set of equations suitable for 3-D simulations, which is more likely to solve more puzzles in the outflow morphology.

1.2 The state of AGB stars

It's important to discuss the general properties of AGB stars first. It helps us to understand why it is fit to have mass loss at this stage. In this section, only the general behavior of an AGB star is considered. Low mass stars have a mass range from 0.8-1.0 $M_{\odot}$ to 2-2.3 $M_{\odot}$ (Iben & Renzini, 1983). Chabrier & Baraffe (2000) sets an even lower limit 0.08 $M_{\odot}$ to distinguish low mass stars from brown dwarfs. Nevertheless low mass stars consists most of the stellar population in the universe (Kroupa, 2002). Intermediate mass stars have a mass range from 2.5-3 $M_{\odot}$ to 8-9 $M_{\odot}$. They have common phases like red giant branch (RGB) and asymptotic giant branch (AGB) when stars are big and surface gravity is low. Mass loss has been detected for both phases (Origlia et al., 2002; Dupree, 1986), but the mechanisms for RGB mass loss is not clear. This thesis focuses on the AGB mass loss stage.

First of all, an AGB star is very big. Figure 1.1 shows the Hertzsprung-Russell diagram ($logT_{eff}$ vs $logL$, HR diagram) of a star with initial mass 2.0 $M_{\odot}$. For comparing the size of the star, some mid-ranged values are picked at the corresponding regions for Main-sequence, RGB

and AGB stars shown in Table 1.1. As we can see, the size of the star keeps increasing along the evolution with main sequence phase smallest and AGB phase largest. Thus the weakest gravitational attraction occurs during the AGB phase.

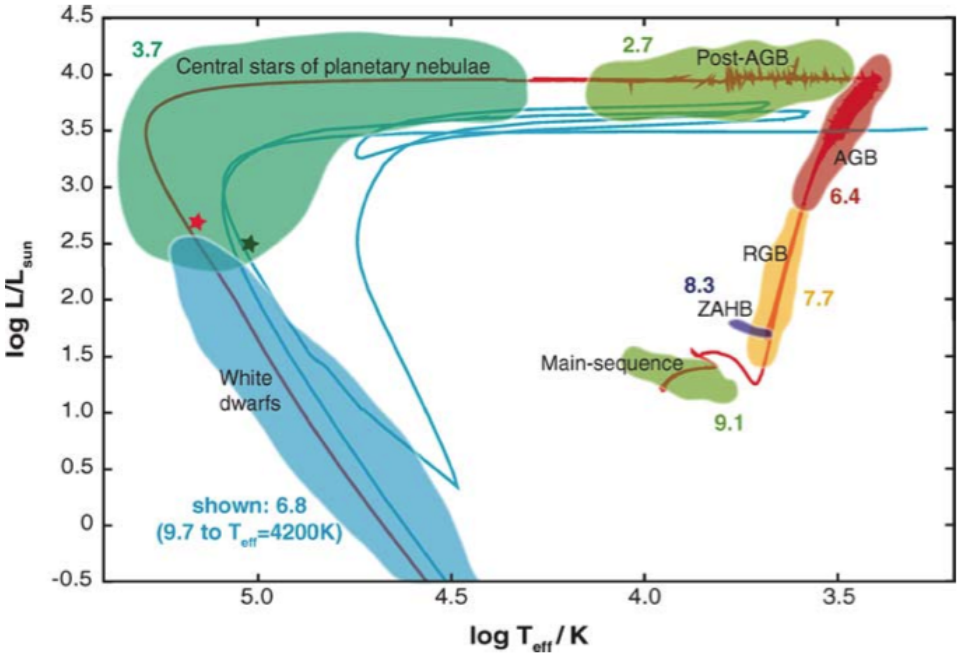

Figure 1.1 Hertzsprung-Russell diagram of a 2 $M_{\odot}$ evolutionary track from the main sequence to a white dwarf. The values in Table 1.1 are picked from the middle of the shaded regions. The numbers beside the shaded regions indicate the log evolution time scales. The blue track shows a possible born-again evolution triggered by a very late thermal pulse. It has been shifted by $\Delta logT_{eff} \sim -0.2$ and $\Delta logL/L_{\odot} \sim -0.5$ for clarity. The graph is from Herwig (2005)

.

Table 1.1 Comparison of Radius, Luminosity, Temperature and surface gravity for the star in Figure 1.1 at different evolutionary phases.

Evolutionary phases	$T(K)$	$L/L_{\odot}$	$R/R_{\odot}$	$g/g_{\odot}$
Main Sequence	6300	30	4.6	0.1
RGB	4000	1000	70	4×10^{-4}
AGB	3100	3000	200	5×10^{-5}

Pioneering works proved that dust and pulsations are very important for generating mass loss in the 70's (Wood, 1979; Hill & Willson, 1979; Willson & Hill, 1979). Pulsating stars are also observed as dust factories and experiencing heavy mass loss (Knapp & Morris, 1986;

Monnier et al., 1998). Later on Bowen (1988); Gail & Sedlmayr (1987) provided basic methods for modeling of mass loss on M and C stars.

The modeling of the interior has been explored by plenty of authors (Wood, 1979; Ostlie et al., 1982; Ostlie & Cox, 1986). The driving zones are located at the hydrogen ionization zone and the first helium ionization zone. The energy transport becomes radiative from the driving zone outside the driving zone. In the Bowen code, the formula from Ostlie & Cox (1986) have been adopted.

$$logP_0 = -1.92 - 0.73logM + 1.86logR \tag{1.1}$$

$$logP_1 = -1.60 - 0.51logM + 1.59logR \tag{1.2}$$

These are linear radial fundamental and first overtone pulsation periods. M and R are in units of the Sun. P is in the unit of days. The nonlinearity of the stellar pulsations does not dramatically change the structure of the star (Barthes, 1998; Ya'Ari & Tuchman, 1996). So the linear equations used here are considered suitable.

The pulsations create shocks in the upper atmosphere. This mechanism enhances the density around the star. Without additional momentum input, this ends up being a ballistic motion. Most material returns to the star (Hill & Willson, 1979; Willson & Hill, 1979; Bowen & Willson, 1991). Near the top of the ballistic motion, radiation pressure plays a important role in supporting the outflow.

Besides having the lowest surface gravity, stars at AGB phase also have the most heavy elements in the atmosphere (Herwig, 2005). Starting from the main sequence phase, a stellar surface consists of mostly hydrogen and helium. These two elements are transparent to radiation in most of the temperature range. The surface material feels negligible radiation pressure at this stage. As a star becomes a red giant following the exhaustion of the hydrogen in the core, the size of the star changes dramatically. This change in size causes the base of the convective envelope to extend into the zones where materials experienced hydrogen nuclear burning. This process is called "first dredge-up"; it produces a change in the surface CNO abundance from C:N:O =1/2:1/6:1 to C:N:O $\cong$ 1/3:1/3:1(Iben, 1967; Iben & Renzini, 1983). Similarly when central helium is exhausted and a denser electron degenerate C and O core is formed for an

intermediate mass star, second dredge-up occurs. Initially more C is brought up to the surface, but after C is processed through the H-burning shell, the final CNO abundances become C:N:O $\cong$ 0.29:0.52:0.86 (Iben & Renzini, 1983). Low mass stars do not go through second dredge-up. Instead, they experience core helium flash which also assists the element-mixing process. At this stage, the star has more oxygen than carbon on the surface. After an AGB star reaches certain luminosity, it starts the thermal pulse phase (TP-AGB). The helium shell burning and hydrogen shell burning take place alternatively, causing a regular change in the size of the star on a time scale of 1000 - 10,000 years. The TP-AGB experiences multiple third dredge-ups as thermal pulses repeat. Depending on the dredge-up efficiency, more C is brought to the outer envelope. The hydrogen shell burning can not convert C into N fast enough. So the surface C abundances keeps increasing and turn the star into S star (C/O$\sim$1) and finally C star (C/O>1) as illustrated in Figure 1.2. Figure 1.3 shows the deepening of the convective zones during different dredge-ups. The material that was once below the hydrogen burning shell containing more heavy elements is mixed into the upper envelope during the third dredge-ups.

These heavy elements are in the gaseous state in the atmosphere where the temperature is above 2000k (Gail & Sedlmayr, 1999). When lifted to cooler regions by the pulsation, they start to condense into dust grains. Dust is very effective in absorbing the radiation and transferring the momentum into the outflow (Willson, 2000; Höfner, 2009). So it is important to study the chemistry in the AGB atmosphere.

According to Figure 1.2, there are three different phases for surface compositions. Early work done by Gilman (1969) provided a wide range of dust species. Recent works by Gail & Sedlmayr (1999); Ferrarotti & Gail (2001, 2002) suggests the dominating dust species are : M-star (C<O): olivine-, pyroxene- and quartz-type silicate dust grains and metallic iron dust grains; S-star (C$\sim$O): metallic iron and quartz-type dust grains; C-star (C>O): carbon, SiC and metallic iron dust grains.

The surface temperature of a AGB star is around 3000K which is a bit high to form a lot of dust. According to Gail & Sedlmayr (1987, 1999), strong condensation only happens below 1500K where the density and radiation are both low in stationary atmosphere. Bowen models produce pulsation induced refrigeration zone which could meet dust condensation condition

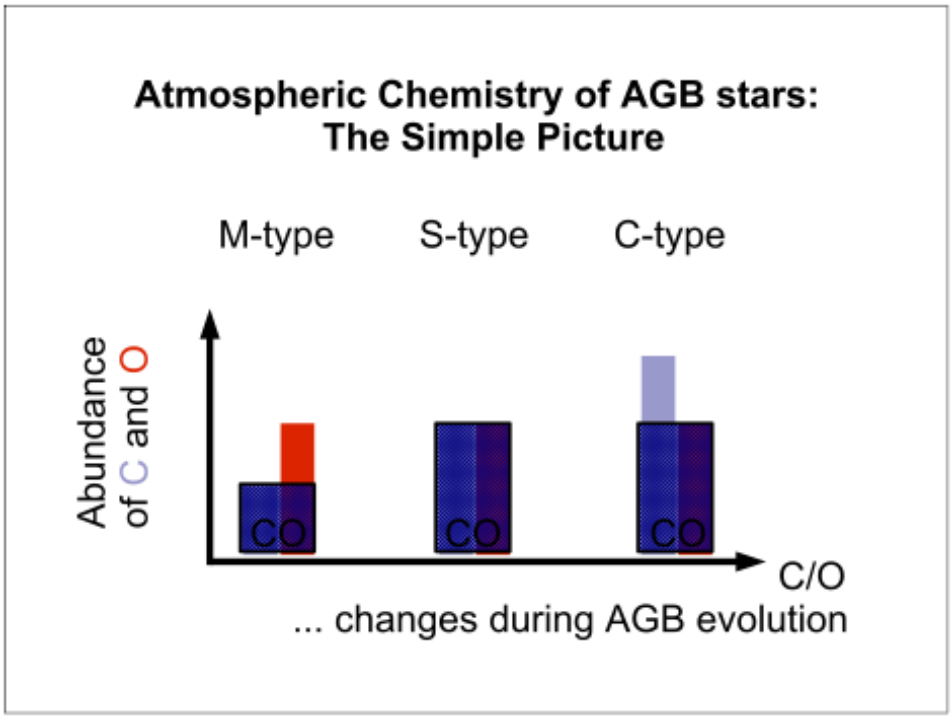

Figure 1.2 This figure shows the relative abundances of C and O in three different phases during AGB evolution. In Chemical equilibrium, the less abundant elements are completely bound in CO, the excess O (M star) or C (C star) is available for molecule and dust grain formations. This graph is from Höfner (2009)

.

around 2-3 R_{AGB} as shown in Figure 1.4. Gail & Sedlmayr (1999); Nuth & Ferguson (2006) suggested nucleation onto seeds from high-temperature condensates as a way of generating dust close to the star. Details of dust condensation will be discussed in Chapter 4.

In this section, I have reviewed some characteristics of AGB stars: low surface gravity, pulsation due to self instability and rich dust content to absorb radiation. With these conditions ready, the low- and intermediate-mass AGB stars will eject their envelopes and end up as white dwarfs.

1.3 Studies on Mass Loss

Mass loss is very important to AGB evolution. Without mass loss, a large fraction of 1.4-10 $M_{\odot}$ stars would blow up as a supernova. Mass loss from intermediate mass stars changes the population distribution of the end product (Willson, 2000). It also has a deep connection with

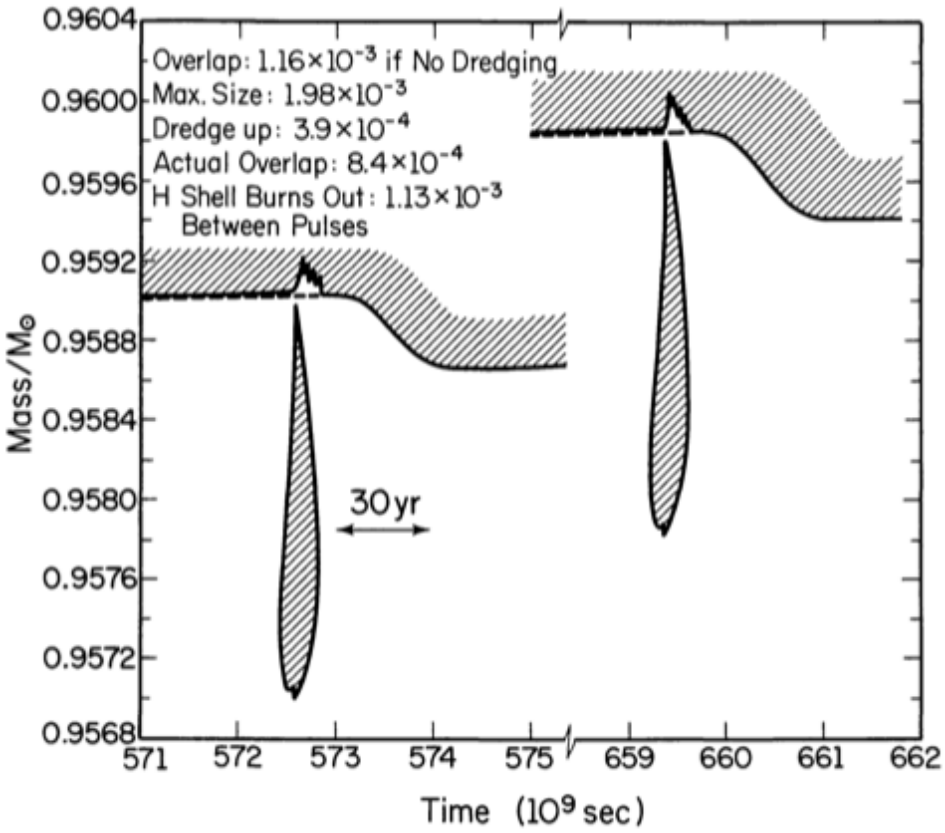

Figure 1.3 The convective regions of $7M_{\odot}$ between 5th and 6th thermal pulses. The shaded region indicates the convective dominated zones. The dashed lines indicate the hydrogen-helium interface before corresponding dredge-ups. This graph is from Iben (1976)

.

studies of the interstellar medium (ISM). It plays an important role in the chemical evolution of galaxies (Dwek, 1998). Here I limited my discussion only to cool stars, because the models involved in my study focuses on AGB stars. For a more complete overview, check Willson (2000); Kudritzki & Puls (2000); Lamers & Cassinelli (1996).

Due to the low temperature in the atmosphere of AGB star, it is hard to directly measure the hydrogen and helium gas around them. Instead, observers detect certain elements from low energy emissions to find out certain characters of the outflow, such as the size of the envelope, the column density of the detected element and the speed of the outflow, etc. From there, they make assumptions about the density or the ratio between the gas and the detected element to calculate the mass loss outflow. These assumptions introduce uncertainties.

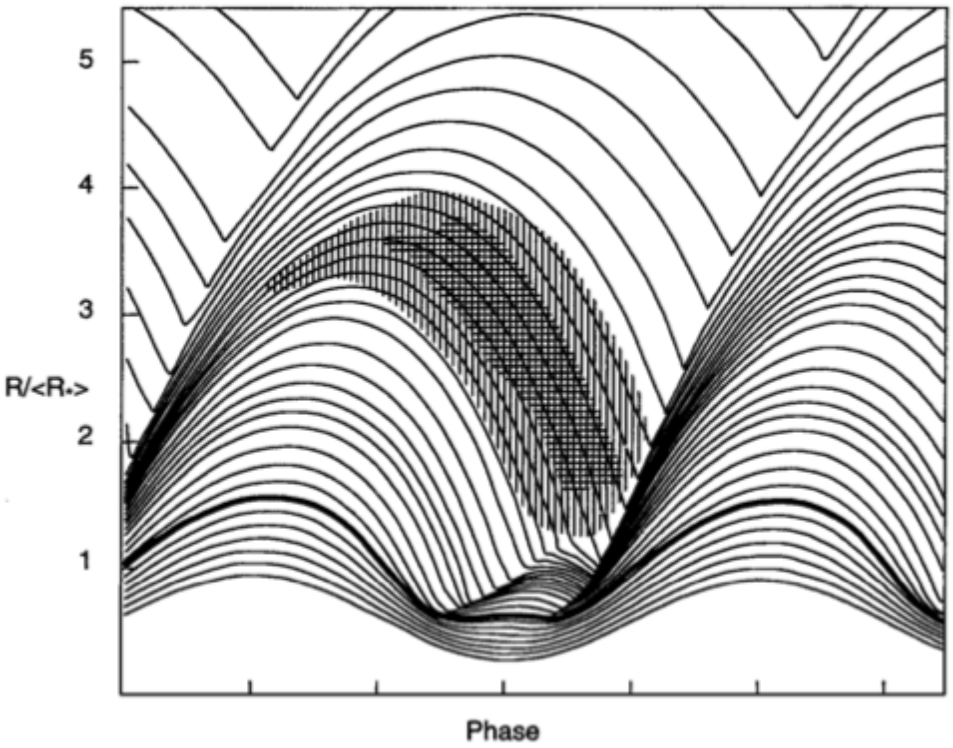

Figure 1.4 This figure shows the pulsation of the atmosphere from the Bowen code. The shaded region has kinetic temperature lower than the radiative equilibrium temperature due to rapid expansion. This provides a region with gas pressure larger than the saturation pressure for dust condensation. Dust may form in this region close to the star. This graph was created by Bowen and appeared in Willson (2000)
.

In optical band, CaII H and K lines absorption can be used to measure the mass loss rate. But the ionization structure of Ca is complicated and can lead to large uncertainties. Early studies using this technical resulted in the famous Reimers formula(Reimers, 1975, 1977):

$$\dot{M} = -\eta \times 4 \times 10^{-13} \frac{L}{gR} M_{\odot} yr^{-1}, \tag{1.3}$$

Reimers equation has been widely used in evolutionary codes for cool stars. But it may not reveal the true of stellar mass loss due to selection effect from observation data (Willson, 2000).

Infrared spectrum is also a good tool to detect dust. Dust shows an infrared excess in the spectrum from 1 - 12μm wavelength (Rowan-Robinson & Harris, 1983a,b). The IRAS catalog provides useful color plots in diagnosing dusty winds. Some important works have been done by Jura (1986, 1987); Knapp et al. (1995) to study mass loss using dust emissions. More recently, Origlia et al. (2002) provided a survey on mass loss from red giants in Tuc 47 using

similar techniques. In M stars, the excessive O forms H_2O which is abundant around these stars. When H_2O flows into the interstellar medium, it is photodissociated by the interstellar ultraviolet radiation and produces OH. Due to self-shielding of H_2O on the OH abundance, the OH concentrates in a shell at a certain distance depending on the mass loss rate and outflow speed (Huggins & Glassgold, 1982; Netzer & Knapp, 1987). Thus by measuring the OH shell density and location and outflow velocity, one can estimates the mass loss rate. By monitoring OH masers, Baud & Habing (1983) developed another empirical mass loss law based on the Reimers equation. CO is another abundant molecules in AGB atmosphere. Due to its high bounding energy, it is common in all three types of AGB stars in section 1.1. Its rotational line emission is very reliable and has been detected from many evolved stars (Knapp & Morris, 1985). It is one of the best indicator of mass loss.

As the variety of the observational data increases, other empirical relations were found by fitting different stellar parameters. Nieuwenhuijzen & de Jager (1990) investigated the dependence of mass loss on M, R and L with a sample of 247 stars and found the following relation:

$$-\dot{M} = 9.6310^{-15}(L/L_{\odot})^{1.42}(M/M_{\odot})^{0.16}(R/R_{\odot})^{0.81}M_{\odot}yr^{-1}. \tag{1.4}$$

Vassiliadis & Wood (1993) developed another empirical relation based on the pulsation periods. For $M < 2.5M_{\odot}$,

$$log\dot{M}(M_{\odot}yr^{-1}) = -11.4 + 0.0123P(days). \tag{1.5}$$

For $M > 2.5M_{\odot}$,

$$log\dot{M}(M_{\odot}yr^{-1}) = -11.4 + 0.0123(P(days) - 100(M/M_{\odot} - 2.5)). \tag{1.6}$$

The four empirical equations for mass loss are plotted in Figure 1.5. They all fit to their corresponding data set, but they are all different by a lot in certain regions. This implies dependence on more stellar parameters which are not showing up in the empirical equations. Empirical relations usually suffer from selection effects Bowen & Willson (1991); Willson (2000). But the mass-losing stars are always obscured by dust shells, and their sizes constantly changing due to pulsations. It's really hard to get accurate measurement of M, L and R for these stars.

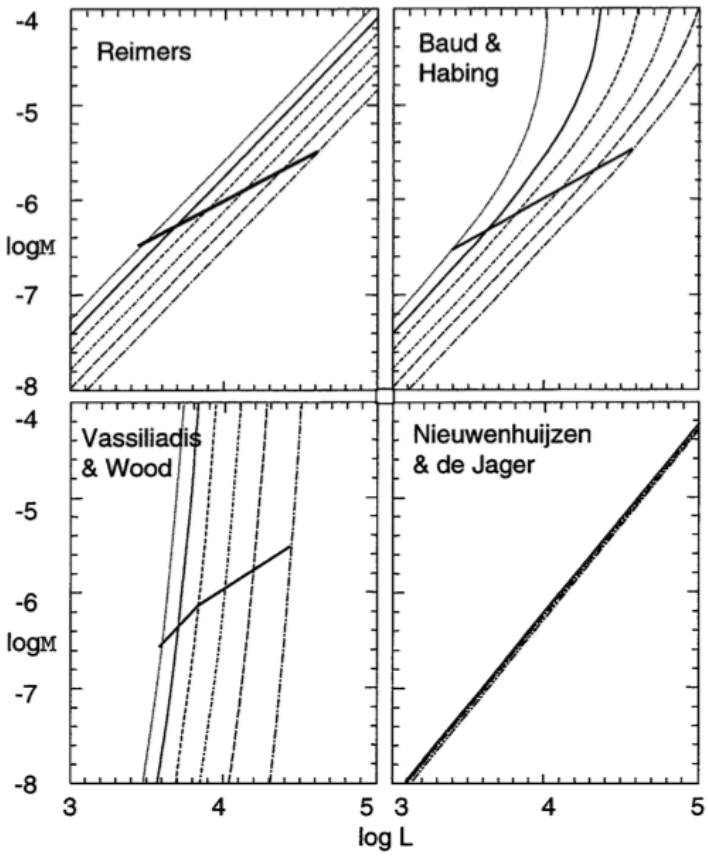

Figure 1.5 Mass loss rate vs. luminosity for four empirical relations. In the first 3 panels, M= 0.1, 1, 1.4, 2, 2.8 and $4M_{\odot}$. In the fourth panel, M = 5, 6 and $8M_{\odot}$ are added since the equation is suitable for more massive stars. The line cross the curves shows the location of deathline, which is described in Figure 1.7. This graph is from Willson (2000)

.

On the other hand, astronomers have made great progress in predicting stellar parameters in AGB evolutions. These parameters can be connected to the mass outflows in theoretical studies. Early works done by Parker in 1960's provide a solid background for stationary solar type winds. But it has been long proven out of connection with giant star outflows. Theoretical works all proved that the dust and pulsation can potentially input momentum into the atmosphere and enhance the outflows. At the same time, most mass losing cool stars are pulsating and surrounded by dust. So the pulsation and dust driven wind theory is the main stream (Willson, 2000; Höfner, 2009).

Wood (1979); Hill & Willson (1979); Bowen (1988) studied time dependent dynamical

models of pulsating atmosphere and dust driven winds. These models use parameterized dust and gas opacities without considering the detailed chemistry in the atmosphere. They are good for predicting mass loss rates giving reasonable conditions but weak in distinguish dust types in M-, S- and C-stars. Bloecker (1995) took models from Bowen (1988) and fitted to a power law to estimate mass loss rates for AGB evolution studies. Arndt et al. (1997) used the code of Fleischer et al. (1992) to calculate mass loss rate for C stars. The corresponding mass loss formulas are plotted in Figure 1.6.

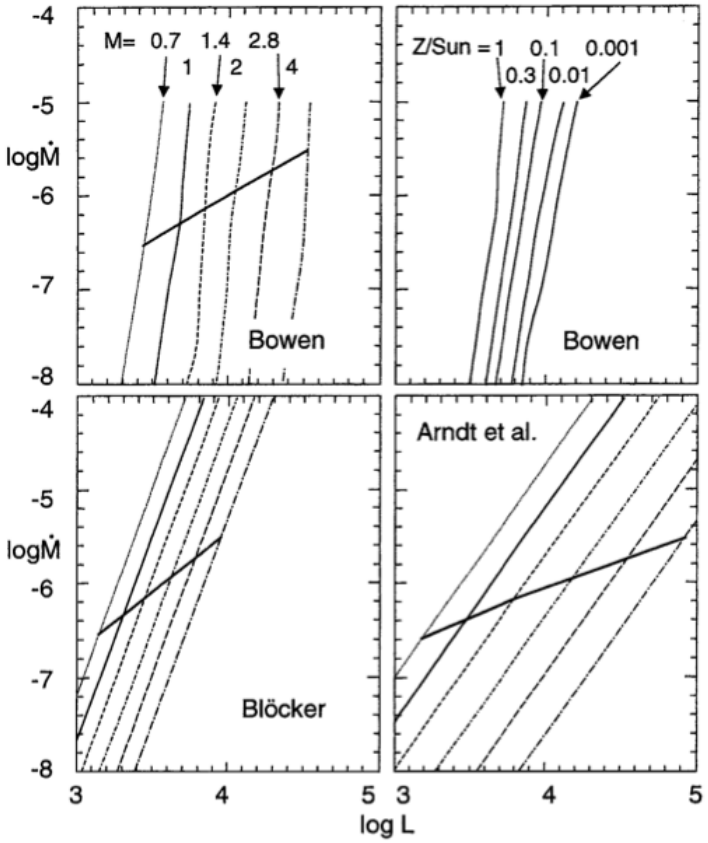

Figure 1.6 Mass loss rate vs. luminosity for theoretical mass loss relations. The deathline is shown in the middle as in Figure 1.5. This graph is from Willson (2000)

.

We can define a deathline by $\dot{M}/M = \dot{L}/L$, where the mass loss starts to dominate the AGB evolution. The deathzone is a range of luminosities around deathline with the corresponding mass loss rate $0.1 \times \dot{M}_{death} < \dot{M} < 10 \times \dot{M}_{death}$. The deathzone is a transition region between the normal AGB evolution and mass loss phase. Before the deathzone, the mass loss rate is very

low and does not affect the evolution. After the deathzone, stars lose most of their envelope, then evolve towards white dwarfs. The deathline for Bowen models is presented in Figure 1.7.

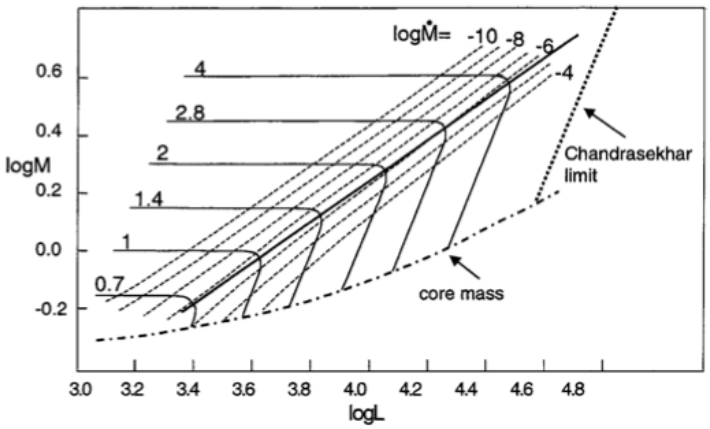

Figure 1.7 The evolution of mass and luminosity for solar composition stars experiencing heavy mass loss. There is a sharp "corner" where stars change their evolution phase. This graph is from Willson (2000)

.

Mass loss models with dust species are also of great interest to astronomers. They provide a population of elements and molecules which is very useful for spectrum studies. C-type stars have been most extensively modeled because lots of lab data are available for carbon condensation. Early studies focused on dust formation and chose a stationary wind (Gail & Sedlmayr, 1988; Gauger et al., 1990). This quickly turned into time-dependent radiative hydrodynamics with pulsation in dust formation models (Fleischer et al., 1992). These models showed an instability due to exterior κ mechanism, which could generate multiple circumstellar shells (Fleischer et al., 1995; Hoefner & Dorfi, 1997; Dreyer et al., 2011). Another instability caused by grain drifting velocity and dust formation was also investigated by Simis et al. (2001) as a possible mechanism for forming large scale structures. ‘ M-stars have been less studied due to the complications of the dust chemistry. Gail & Sedlmayr (1999) and Ferrarotti & Gail (2001, 2002) made important suggestions about the dust species available in oxygen rich stars. Woitke (2006a) found that the radiative acceleration of O-rich dust is too weak to give significant dust driving, but Höfner (2008) solved this problem by introducing micron-sized iron-free olivine-type grains. Her results yielded satisfactory mass loss for M stars. S stars are rarely considered in theoretical studies due to the expected lack of dust; the expectation for

dust species in S stars were studied by Ferrarotti & Gail (2002).

Using a mass loss formula, AGB evolution studies can take the mass variation into consideration (Wachter et al., 2002; Marigo & Girardi, 2007) for a better understanding of the final product. In chapter 2, we present a mass loss study covering a wide range of parameters using the Bowen code. This improved mass loss formula will give astronomers better insight into this mass loss phenomenon.

CHAPTER 2. The Bowen code and mass loss

In this chapter, the Bowen code and its setup are briefly described. The ongoing modeling of mass loss for a large grid of pulsating stars and modeling parameters is discussed. Finally, a study of the dust grain life cycle through shocks is carried out using this code.

2.1 The Bowen code

The Bowen code is built on a Lagrangian grid. There is no mass transfer between grid cells and the grid size can change dynamically. The radiative equilibrium temperature is calculated based on a spherically grey atmosphere approximation. The gas temperature is determined by the dynamics of the gas, the hydrogen cooling at high temperature, the dust heating and cooling and the density-dependent heating and cooling. The critical density is defined by $\frac{Q}{Q_{RE}} = \frac{1}{1+\rho_{crit}/\rho}$. Q and Q_{RE} are the actually and equilibrium heating and cooling of the gas. At low density, cooling and heating by radiation are both inefficient. Beside pressure and gravity, dust and molecules also absorb radiation and transfer momentum into the gas. The dust and molecular opacities are considered grey opacities with parametrized temperature dependence. The advantage of the Bowen code is that it is easy to adjust and fast to run, but it lacks details of the dust formation process and can not be used to compute the spectrum from the outflow. It has also been suggested (Höfner, private communication) that (a) the mean opacity we have used for most models is too low, giving an atmosphere that is too massive; (b) the grey approximation does not take into account essential physics of the wind mechanism. In our large grid, we test the effects of varying the opacities.

The Bowen code is a 1-D code, dividing the atmosphere into concentric spherical zones at specific position R. Rotation and magnetic effects are assumed negligible. Standard finite-

difference methods are used following the equations in Ritchmyer & Morton (1967). The zones are set up based on Lagrangian coordinates and solved by explicit integration. Time steps are calculated in each step by taking the smallest of 3 constraints. (1) Δt <P/200, (2) $\Delta t < 0.6 * (\Delta r / v_{sound})$, (3) Volume change $\Delta V/V < 0.2$.

The ideal gas law is used with a constant mean molecular weight $\mu = 1.26$. It is assumed that γ=5/3. The radiative equilibrium temperature T_{RE} is calculated using the spherical Eddington approximation for a gray atmosphere Chandrasekhar (1934). The gas opacity, κ, has been assumed to be uniform. The radiative equilibrium temperature is found for all zones, even those out of radiative equilibrium, because dynamical cooling is handled as a relaxation towards T_{RE}. We expect to be able to use more detailed information to improve the treatment of the gas opacity.

The energy treatment for the gas includes density dependent heating and cooling by radiation, temperature changes due to compression and expansion, and heating or cooling by interaction of the gas with the dust. The dust is assumed to be at the appropriate radiative equilibrium temperature taking into account the albedo function for silicates. (So far, we have not consider carbon-based dust.) This leads to the different temperatures for dust and gas. Even though shock waves may dramatically increase the gas temperature, shocks do not necessarily destroy the dust within the gas; this leaves more dust in the post-shock material and helps accelerate the mass loss.

Recent discussions (Höfner, 2009) suggest that the composition of dust in both carbon and oxygen-rich Mira atmospheres is a mixture of carbon-based and silicate grains. We expect to be able to use the Bowen code to explore the effects of various non-equilibrium mixtures of dust parameters on the winds.

2.1.1 Mass loss rate study

In collaboration with Lee Anne Willson, I have generated a large grid of models using the Bowen code to test the mass loss rate. These models cover a parameter space shown in Table 2.1.

The condensation temperature is the temperature when half of the heavy elements condense

Table 2.1 The parameter space used to test mass loss rate.

Mass (M)	0.8, 1.0, 1.2, 1.4, 1.7, 2.0 $M_{\odot}$
Metallicity (Z)	0.02, 0.002, 0.0002 0.00002 Z_{odot}
Mixing Length (l/H)	0.7, 0.9, 1.1
gas opacity (κ)	0.0004, 0.004, 0.04 cm^2/g
critical density (ρ_{cx})	10^{-10},10^{-11},$10^{-12} g/cm^3$
condensation temperature (T_{cond})	1150, 1250, 1350, 1450 K
Piston power adjustment (P_p)	0.9, 1.0 , 1.1

into dust grains. These temperatures are used to fit the Si dust behavior in O stars. The piston power adjustment is variation the piston power in the Bowen code. This parameter space gives us a better understanding of how mass loss rate depend on properties of the star (L, M, R, Z) and the physical processes in the models ($\rho_{cx}, T_{cond}, \kappa, P_p$). The results will be published in Willson et al. (2011).

2.2 Life cycle of dust in a pulsating atmosphere

In a pulsating atmosphere, the conditions in the refrigerated zone fits the conditions expected to lead to dust formation as mentioned in Chapter 1. Here I did some preliminary tests on the carbon dust life cycle using the Bowen code to determine the density, kinetic temperature as a function of the phase and radial pulsation. The model parameters are shown in Table 2.2.

Table 2.2 The stellar parameters used to test the dust life cycle.

Mass	1 $M_{\odot}$
Luminosity	3000 $L_{\odot}$
R	189 $R_{\odot}$
T_{eff}	3105K
Period	207 days
Amplitude	2.2 km/s

This model satisfies Eqn. 1.1 . The resulting mass loss calculated from Bowen's code is $10^{-9} M_{\odot}/yr$. Four zones (21, 46, 71, 96) are plotted in Figure 2.1. Zone 21 is set to be the photosphere of the star. Zone 96 is where R = $2R_{star}$. The middle zones are evenly placed. The first figure shows the gas temperature and dust temperature evolution in each zone. Since

dust is considered a blackbody, it carries the equilibrium temperature. The gas temperature is dynamic. Near the photosphere, the density is high and the non-LTE effect is weak, so the temperature difference is small. At zone 46, the density has dropped by an order of 2 (1% of photosphere), and the difference between gas temperature and dust temperature is significant. A refrigerated zone is created after a strong shock, generating the lowest kinetic temperature of the 4 test zones. In zone 76 and 96, the kinetic temperature is obviously higher than the equilibrium temperature. This is due to the mechanical heating by the shocks and the lack of cooling in thin gas.

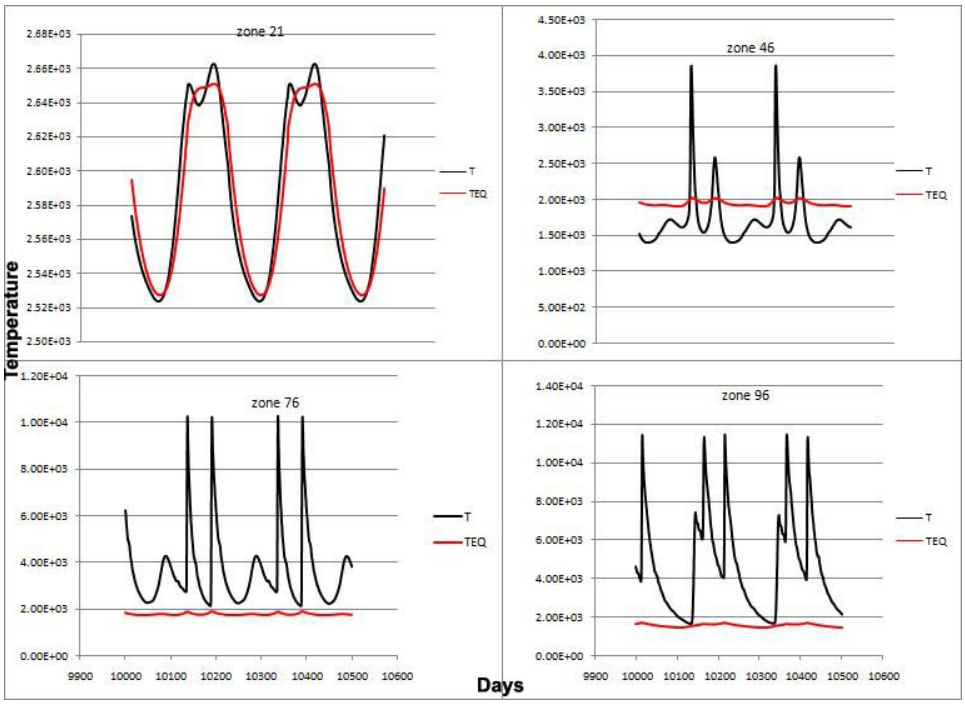

Figure 2.1 This figure shows the gas temperature (T_{kin}) and dust temperature (T_{RE}) oscillations vs. time in 4 test zones.

The time scale for dust to form under conditions similar to those obtaining near 2 R_{star} is about 10^6 sec, about 0.1 of the pulsation time scale. Thus, the dust grains have enough time to form in the refrigerated zone. Once the grains form they will tend to stay in equilibrium with the radiation field, with $T \sim T_{RE}$, but will be losing material from collisions with the gas. The net evaporation rate will depend on both T_{dust} and T_{kin} in the gas. The non-LTE temperature structure produces a refrigerated region where the grains can form easily and quickly, but also

produces high gas kinetic temperatures for longer than in the LTE models. The question we are investigating is under what conditions, if any, do the grains in a non-LTE model survive from one cycle to the next.

Figure 2.2 shows the carbon density and critical cluster size evolution in zone 46 during the same time span as shown in Figure 2.1. All the quantities are calculated using the moment methods described in Chapter 4. The carbon density is normalized to its initial value for better demonstration of condensation percentage. The carbon density shows a wide window where dust is available in the refrigerated zone. The transition between no dust and complete condensation is very narrow, consistent with the critical temperature approach to the onset of nucleation used in the Bowen code.

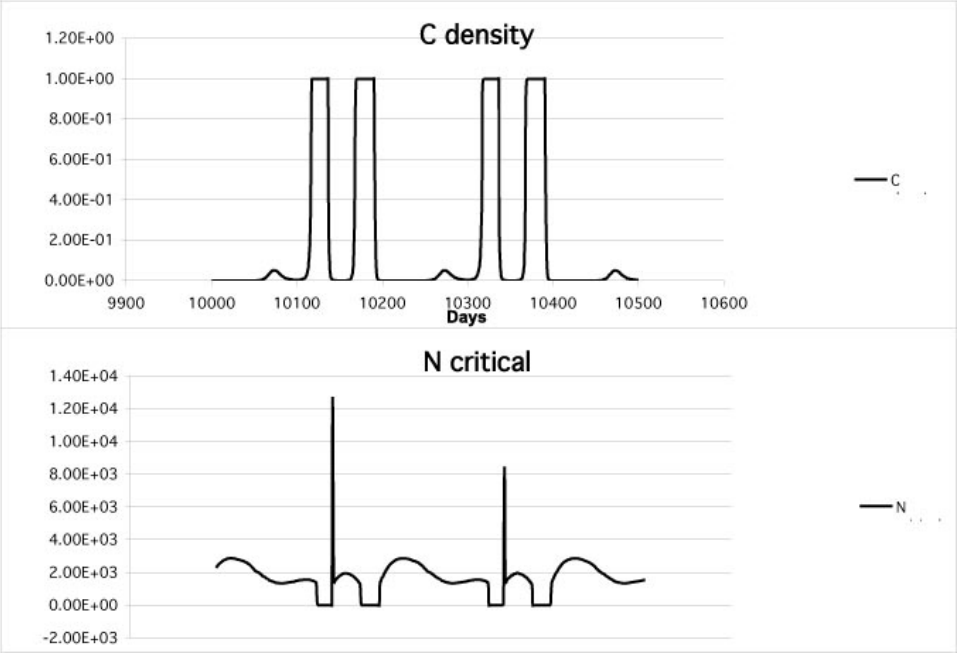

Figure 2.2 The top panel shows the normalized carbon density vs. time. The bottom panel is the critical cluster size vs. time.

This work shows that carbon dust can only survive briefly in the pulsating star atmosphere. Since carbon grains are the toughest grains among other species Ferrarotti & Gail (2002). No dust could survive the shocks and grow very large. But since they are close to the star, they absorb more radiation and better accelerate the outflow. I hope improve the modeling as described in Chapter 4 for a better picture.

CHAPTER 3. Multiple spiral arms around AGB stars

The phenomenon of multiple spiral arms was discovered by accident. The addition of a small mass companion was originally designed to induce more mass loss, since the gravitational attraction of the companion can also lift the surface material. The over all impact on the surface of the star is quite small and a super Jupiter mass companion does not stimulate a lot of mass loss. However, an interesting resonance pattern was discovered as a result from their interaction. This is the excitement of scientific research.

3.1 Introduction

One of the great puzzles associated with AGB and post-AGB evolution is the presence of multiple shells and rings in planetary nebulae (PNe) halos and around some AGB stars. With the help of Hubble Space Telescope (HST), more details in the halos of PNe have been revealed. Rings with time scales ranging from decades up to hundreds of years are stunningly clear in CRL 2688 (Sahai et al., 1998) and IRAS 17150-3224 (Kwok & Su, 1998). For short reviews, check Corradi et al. (2004) and Terzian & Hajian (2000). The mechanism that produces these time scales remains a challenge. The intrinsic fundamental pulsation periods and thermal pulsing time scales (helium shell flash time scale) are either too small or too large for this purpose. While the Kelvin-Helmholtz time scale has the right order, no mechanism operating on that time scale has been found. A lot of effort has been expended trying to explain this phenomenon, for a review, check Bond (2000) and Balick & Frank (2002) for reviews. Most of the previous models could generate discrete shells, but the computed structures are not periodic. Successful modelings are binary perturbation mechanisms by Mastrodemos & Morris (1999) and Harpaz et al. (1997) for periodic structures, multi-fluid modeling with dust instability by Simis et al.

(2001) and exterior κ mechanisms by Dreyer et al. (2011). The binary models done to date involve study large companions that are relatively far away. The effects of small companions (several $M_{Jupiter}$, $m/M_{star} < 0.1$) have remained unexamined. The purpose of our study here is to investigate the influence of a small and close companion on the outflow.

In this paper, we present a new set of models computed with the hydrodynamic atmosphere/ mass loss code by Bowen (Bowen, 1988). In these models, the atmosphere outflow is generated by a combination of pulsation and radiative acceleration. Pulsation leads to the formation of shocks above the photosphere. Without a companion, the shocks becomes insignificant at about 10 stellar radii (∼10AU) (Willson et al., 2011). When perturbation by a small companion is introduced, these shocks cluster into longer periodic spiral arms. These spiral arm periods, which equals to the spatial separation of spiral arms divided by the wind speed, can be different from either pulsation period of the central star or the orbital period of the companion. The details of the period coupling are discussed in section 4. In most models, both orbital period and pulsation period are smaller than the spiral arm period.

3.2 Modeling methods

3.2.1 The Bowen code

The Bowen code (Bowen, 1988) was originally designed to model mass loss from oxygen-rich AGB stars. It assumes spherical symmetry for both the interior (not computed) and the atmosphere (included to a few scale heights below the photosphere). The code applies 1-D zoning to this spherically symmetric atmosphere. The hydrodynamic model assumes an ideal gas equation of state and the first law of thermodynamics. Due to the low density of the gas in the stellar outflow, thermal relaxation is not very effective, and the gas kinetic temperature (T_{kin}), the radiative equilibrium temperature (T_{RE}), ionization and excitation temperature can all differ. The code uses a density-dependent thermal relaxation equation to treat the non-LTE coupling of the gas and the radiation field. Dust and molecules are available in cool regions for absorbing radiation and transferring momentum to the outflow (Gilman, 1972). A sinusoidal piston is set below the photosphere to simulate the pulsation of the star. Artificial viscosity

is also used to treat shocks. The dust and molecular formation are instantaneous functions of T_{RE} and T_{gas} assuming the time scales to form dust and molecules are much smaller than the dynamical time scale. The maximum dust and molecular opacities are set to $2cm^2/g$ and $0.4cm^2/g$.

The parameters of the central star used in theses calculations are listed in Table 3.1. These correspond to 1-$M_\odot$ near the tip of AGB (Willson, 2000). Given luminosity L_{star}, mass of the star M_{star}, and metallicity Z, we can use a formula from Iben (1984) to find the radius:

$$R_{star} = 312(L_{star}/10^4)^{0.68}(1.175/M_{star})^{0.31S}(Z/0.001)^{0.088}/(l/H)^{0.52}, \tag{3.1}$$

where L_{star} and M_{star} are in solar units, Z equals abundance by mass of heavy elements and S equals 0 when $M_{star} \leq 1.175 M_\odot$ and S equals 1 otherwise. The mixing-length parameter l/H affects the size of the star at a given L_{star}, M_{star}, Z; we have used $l/H = 0.9$ as was used for prior models (Bowen & Willson, 1991). The effects of varying l/H on the mass loss rate are considered in Willson et al. (2011). The pulsation period is taken from the formula by Ostlie & Cox (1986) for fundamental mode,

$$P_{puls} = 0.012 M_{star}^{-0.73} R_{star}^{1.86}, \tag{3.2}$$

where M_{star} and R_{star} are in solar units. We selected the pulsation amplitude to give an average piston power 0.01 of L_{star}. This is a reasonable assumption since it is easy for the star to drive the pulsation at its current luminosity. $V_{terminal}$ is the terminal velocity of the wind without a companion; for all models calculated here, it is constant beyond $12R_{star}$. For more details of the modeling, see Bowen (1988); Willson et al. (2011).

3.2.2 The properties of the companion

We assume the companion revolves in a circular orbit with a fixed distance to the center of the star. For the purpose of this simulation, the companion is small ($M_{comp} = 10M_{Jupiter} = 0.01M_{star}$). Since M_{comp}/M_{star} is much less than 1, in order to influence the outflow in a major way, the companion's orbit must be close to the photosphere. With low mass and low orbital altitude, the effect of the companion is very localized, both spatially and in time at a given

Table 3.1 The central star parameters

M_{star}	$1M_{\odot}$
L_{star}	$5000L_{\odot}$
T_{eff}	$2966K$
R_{star}	$267.8R_{\odot}$
Pulsation period	$394days$
Pulsation Amp.	$4.0km/s$
$V_{terminal}$	$9.35km/s$ at $18R_{star}$
$\dot{M}_{star}$	$1.25 \times 10^{-6}M_{\odot}/yr$

location (C. Struck and L. Willson, in prep.). However, the orbital radius cannot be constant in reality and is influenced by three factors: the decreasing mass of the central star, gas drag and tidal force. See section 4 for discussion on balancing these factors.

We estimated the companion's size from its mass and the mean density of Jupiter. This gives $R_{comp} = (\frac{M_{comp}}{4/3\pi\rho_{Jup}})^{1/3}$, about 10% of the width of the smallest computational zone that the companion passes through. Thus, the companion acts primarily like a point source of gravity even when it is inside a zone. Its size only matters when the distance between the center of the companion and the center of a zone is smaller than its radius. In that case, we calculate a reduced gravity using $g = (4/3)\pi GD^3\rho_{Jup}/D^2$, where D is distance between the center of the companion and the center of the zone; this prescription avoids singularity at D =0. In the model, we only include the momentary vertical component of the gravitational force from the companion on each computational zone, as the horizontal components before and after the companion passes must cancel out for the 1-D model.

Table 3.2 below lists all the models with different properties of the companions. P_{sa} is the spiral arm period which is discussed later.

3.3 Results

In the following subsections, we show the effects of the companion and the origin of the spiral arms. A comparison of slices of atmospheres at various times reveals that the structures of the shocks are dependent upon the mass of the companion. The equatorial outflows of different models show the multiple spiral arms.

Table 3.2 The companion parameters

Model	$M_{comp}(M_{Jupiter})$	Distance(R_{star})	$P_{orb}(days)$	Spiral arms	P_{sa}/P_{puls}
1	2	1.019	522.43	4	60
2	5	1.019	522.43	4	60
3	5	1.1	586.1	3	60
4	8	1.1	586.1	3	60
5	10	1.1	586.1	3	60
6	12	1.1	586.1	3	60
7	10	1.325	775.08	2	60
8	10	1.339	786.94	2	60
9	20	18.187	39400	1	100

3.3.1 The effect of the companion

When the companion passes a particular region on the stellar surface, the atmosphere below is temporarily pulled upward. This stretching of the atmosphere causes the gas kinetic temperature, T_{kin}, to decrease in the expanding zones. Figures 3.1 and 3.2. show the differences in this refrigeration effect between stronger shocks and weaker shocks. The star itself is pulsating, creating motion in the atmosphere. When the companion approaches while the shock wave is going up, the companion works on the dense post shock material creating stronger shocks. For example in Figure 3.1, the companion passes at time = 251.12 cycles, right in the middle of the rising wave. On the other hand, in the weaker shock region, the companion's attraction is strongest where the atmosphere is most extended with low density. Since the companion passes at constant speed, these regions receive similar acceleration from the companion and end up with similar speed. So the region behind a weak shock carries less momentum than that behind strong shocks . The weak shocks decelerate more quickly than strong shocks when they go through the atmosphere and collect infalling material. For example in Figure 3.2, at time = 291.23 cycles, the pull of the companion only creates a tiny tail which falls back very quickly. Behind each shock, the lighter region indicates a cooler zone where T_{kin} is lower than T_{RE}. The strong shocks have a much long-lasting cooling effect than the weak shocks do. Right behind the shock front, where the gas is most compressed, the dark color represents high T_{kin} up to 10,000K.

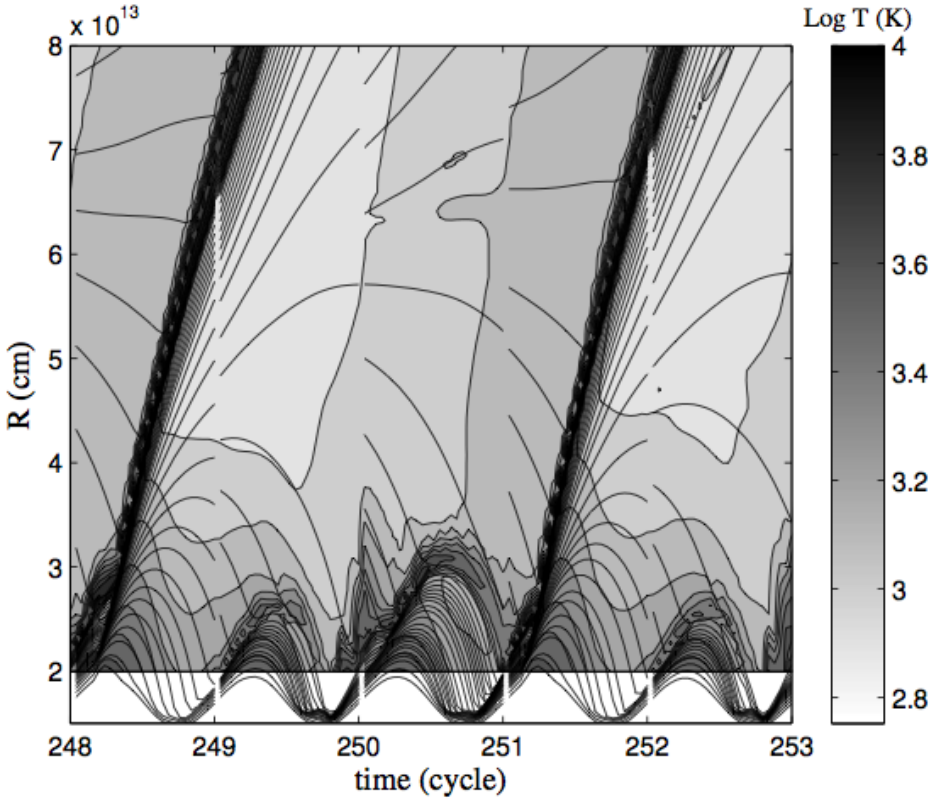

Figure 3.1 Kinetic temperatures in the vicinity of the stronger shocks for Model 5. Contours of kinetic temperatures are superimposed on tracers of computational zones in the models. Zones cluster tightly where shocks appear. Gaps in the zone tracers occur where the model has been rezoned, and dots along the shocks are artifacts of limited sampling in the output file. The contour map is only provided above $2 \times 10^{13} cm$ while the mass motions are traced to deeper levels, hence the artificial boundary of the contour plot. Figure 3.5 shows a more extended region of the same model, Model 5.

3.3.2 The origin of the spiral arms

The shocks create refrigeration zones that increase the abundance of molecules in the lower atmosphere but not the amount of dust in this code. Figure 3.3 shows the relationship between shocks and molecular acceleration in the atmosphere. Since molecules are sensitive to T_{kin}, molecules are destroyed along the hot shocks and reformed below the shock in the refrigerated zones. Periodic patterns in molecular acceleration are caused by the periodic change in the radiation intensity as the star pulsates, which leads to varying radiation pressure on the molecules. The dark regions indicate high molecular acceleration; these regions are close to the

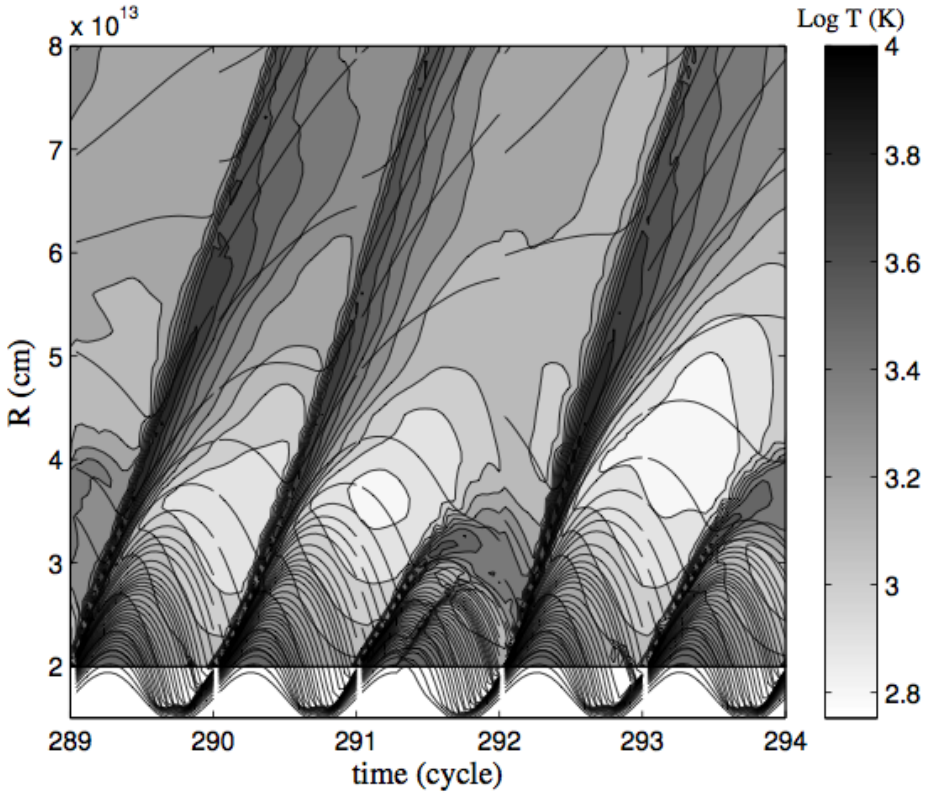

Figure 3.2 Kinetic temperatures in the vicinity of the weaker shocks for Model 5 as Figure 3.1 and Figure 3.5. Because the planet passes at a different pulsation phase, the shocks are not as strong as in Figure 3.1.

photosphere in the post shock regions where T_{kin} is lower than T_{RE}. Strong molecular acceleration only occurs above 2AU; no significant molecular acceleration exists near the origin of the shocks. On the other hand, dust is more effective than molecules at absorbing and emitting energy in the form of radiation. The code assumes that the dust stays at T_{RE} even inside the shocks and thus is not destroyed. We neglect the dust destruction in the hot shocks for 2 reasons: 1) hot shocks occur mostly below $2R_{star}$ while dust grains exist above that (Figure 3.4); 2) We assumes instantaneous dust formation depending on T_{RE}. The narrow shocks appear every couple years do not reduce the dust significantly in our simulation. In Figure 3.4, the dust acceleration also varies as the star pulsates and this acceleration continues above 3AU. So molecular acceleration and dust acceleration do not help to initiate shocks. It is the pulsation of the star and gravity from the orbiting companion that shape the initial shocks.

After the shocks are initiated, radiative acceleration acting on grains and molecules transfer

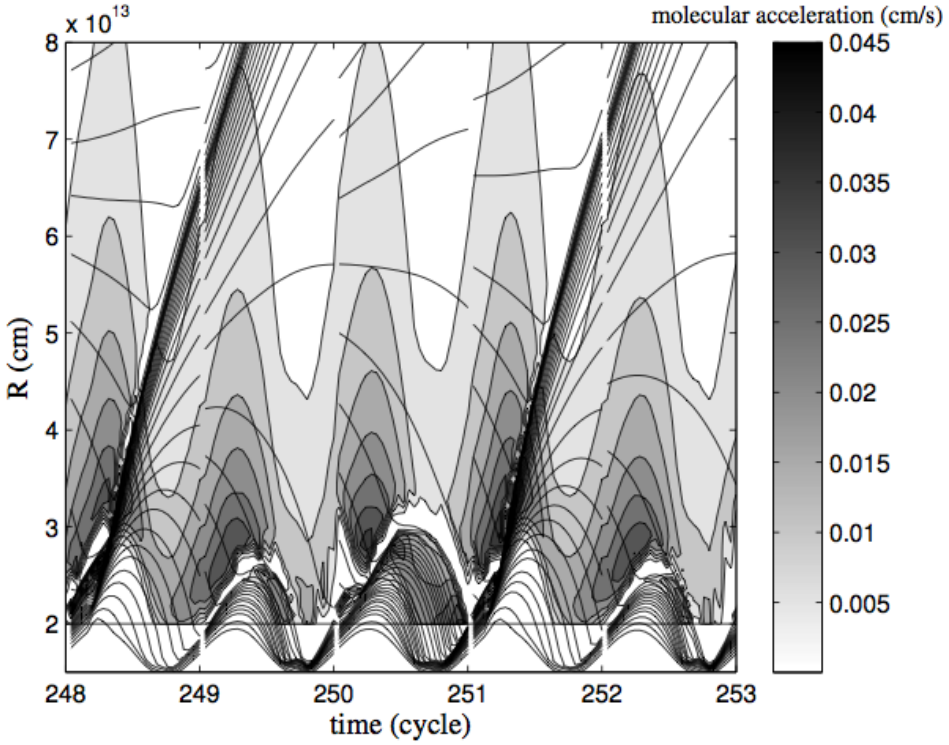

Figure 3.3 Molecular acceleration for the same model vs. times as Figure 3.1. The low molecular acceleration between cycles 250 and 251 near $2.5 \times 10^{13} cm$ is due to the destruction of molecules by the rising shock. Additional molecules also show up at the same time below the shock due to extra cooling by expansion. Note the similarity with T_{kin} (Figure 3.1). The periodic pattern in the molecular acceleration between cycles is caused by luminosity variations as the star pulsates.

momentum into the outflow. Figures 3.5 and 3.6 show the difference between outflows with different dust and molecular opacities. Figure 3.5 shows the results for the normal values among all models while Figure 3.6 shows the results when dust opacity and molecular opacity have 1/5 and 1/2 of their standard values. Both figures carry the same color map. On the left side of Figure 3.5, the strong shocks all move out together and later cluster into a spiral arm. On the right hand side, the weak shocks leave only a very faint mark in the upper atmosphere. In Figure 3.6, the strong shocks decelerate significantly below $1 \times 10^{14} cm$, and most of the mass is confined below that height. Clearly, dust and molecules play a crucial role in generating these outflows.

To determine the propagation speed of the shocks at a given height, we looked at the arrival

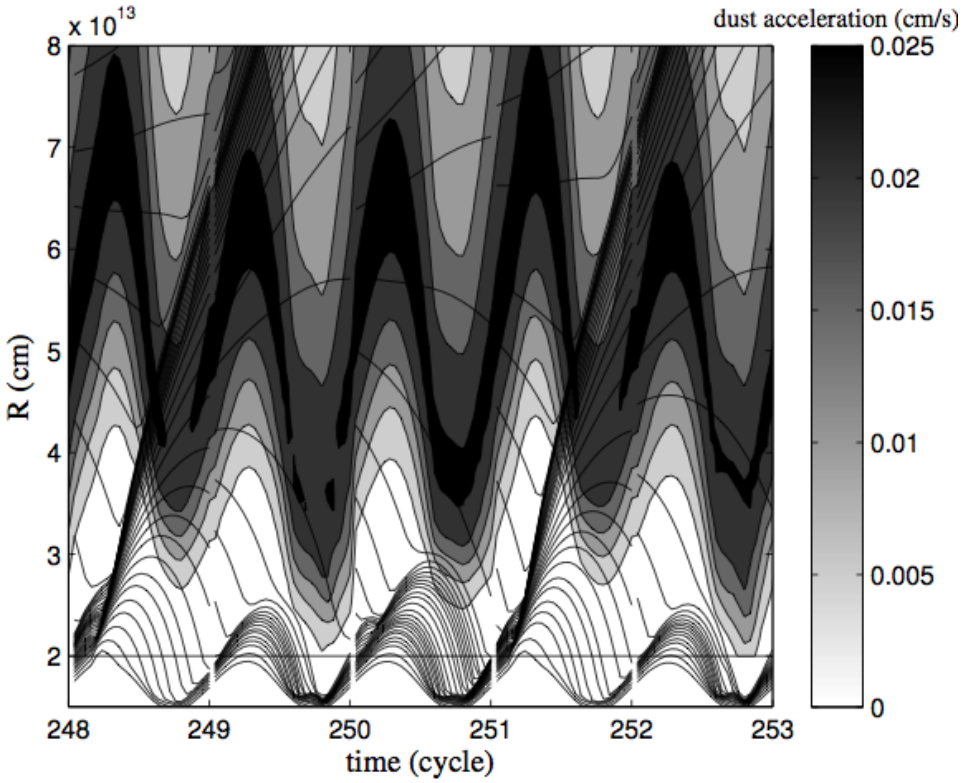

Figure 3.4 Dust acceleration for the same model vs. times as Figure 3.1 and Figure 3.3. Dust appears above 2AU and maintains a periodic pattern as the radiation strength varies. Dust acceleration is more stable than molecular acceleration with time. It provides continuing acceleration from $4 \times 10^{13} cm$ - $8 \times 10^{13} cm$.

time of the maximum density spike vs. height, as is illustrated in Figure 3.7 for a region of 11 layers around $R = 1.45$ to 1.55×10^{14} cm. In the figure, an additional vertical separation in $log\rho$ has been introduced to separate the curves. Table 3.3 lists shock speeds and maximum density for the layer at 1.5×10^{14} cm obtained by this method.

In Figure 3.8, we show why strong shocks travel a lot further than weak shocks. It is a plot of post shock density and shock velocity vs. time. In the strongest shock region the density is more than 2 orders of magnitude higher than the density in the weakest shock region. Even though the shock speed of the weak shock region can be twice as much as the shock speed of the strong shock region, the momentum carried by the material behind the strong shocks is still about 100 times larger. The strong shocks can plow into the in-falling gas without losing too much of their speed, while the weak shocks can not survive and significantly slow down. In

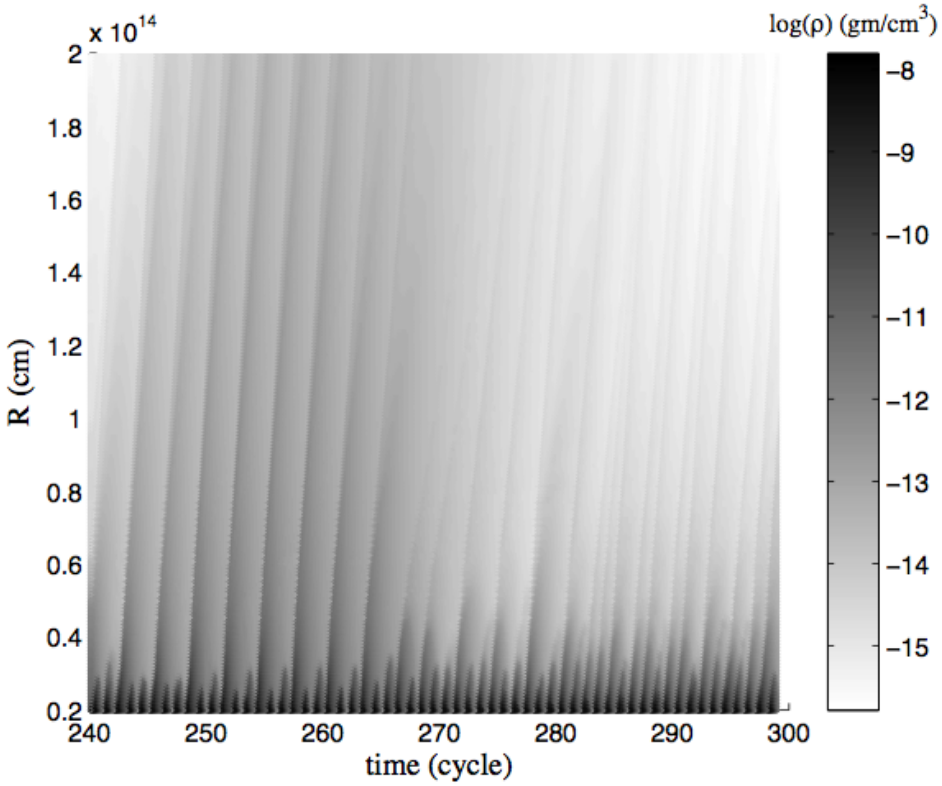

Figure 3.5 Density variation over a spiral arm period (60 cycles). The stronger shocks show up as higher densities to the left. Note that the density contrast persists beyond $2 \times 10^{14} cm$.

addition, given similar composition, the denser outflows associated with the strong shocks tend to have higher optical depths than weak shocks. The optical depth determines the efficiency with which the radiation is converted into momentum of the outflow.

The periodic spiral arm is the result of the clustering of strong shocks. Figure 3.9 contains a density contour map that shows the time evolution of the atmosphere. The spikes on the contours represent shock locations. By connecting the tips with thin lines, we can track the motion of each shock. The slopes of the lines are $V_{shock} = dR_{shock}/dt$. The bold line shows the spiral arm location where shocks cluster together. To the left of the spiral arm, the weak shocks slow down due to the material that is falling back onto the star. To the right of the spiral arm, the shocks are strong and the leftmost shock gets pressure support from its nearby shocks and keeps going to meet the weak shocks at the spiral arm location. The rightmost strong shock decelerates by losing material to the low pressure region below it. This material

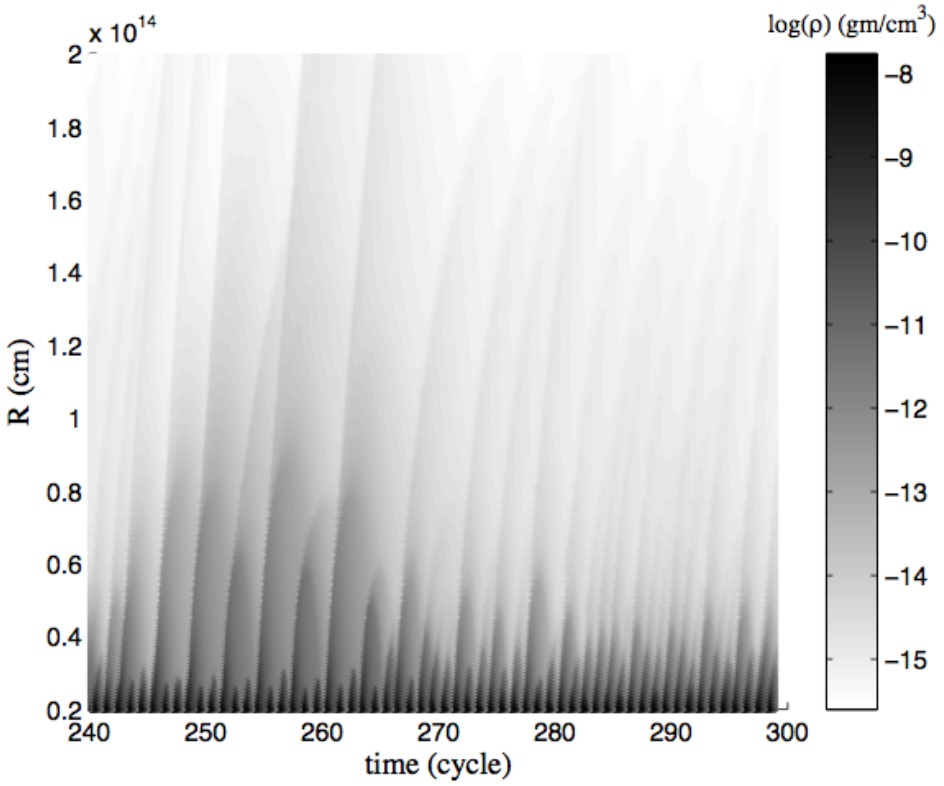

Figure 3.6 The same as Figure 3.5 but for a model with artificially low dust and molecular opacity. With less radiative acceleration the large-scale flow is smoother, and near the star, material fails to escape.

in turn decelerates the next generation of weak shocks and starts another cycle of clustering.

3.3.3 Spiral arm structure and morphology

The structure of the shocks is influenced by both the companion mass and its orbital period. In this section, we describe how the shocks in Models 3 - 6 reveal the relation between the shock structures and the companion masses. Models 1 and 2 show the effect of a companion in a really close orbit. Since Model 1 has the weakest density contrast, we argue that any companion with mass less than 2 $M_{Jupiter}$ is not going to show any trace of interaction in observations. Models 7 and 8 show relation between the spiral arm period and the equatorial disk structure. Model 9 has the largest companion mass and longest orbital period and gives us a clue as to how this mechanism can produce a single spiral arm.

There is a steady trend of narrower and faster spiral arm speed with increasing M_{comp}.

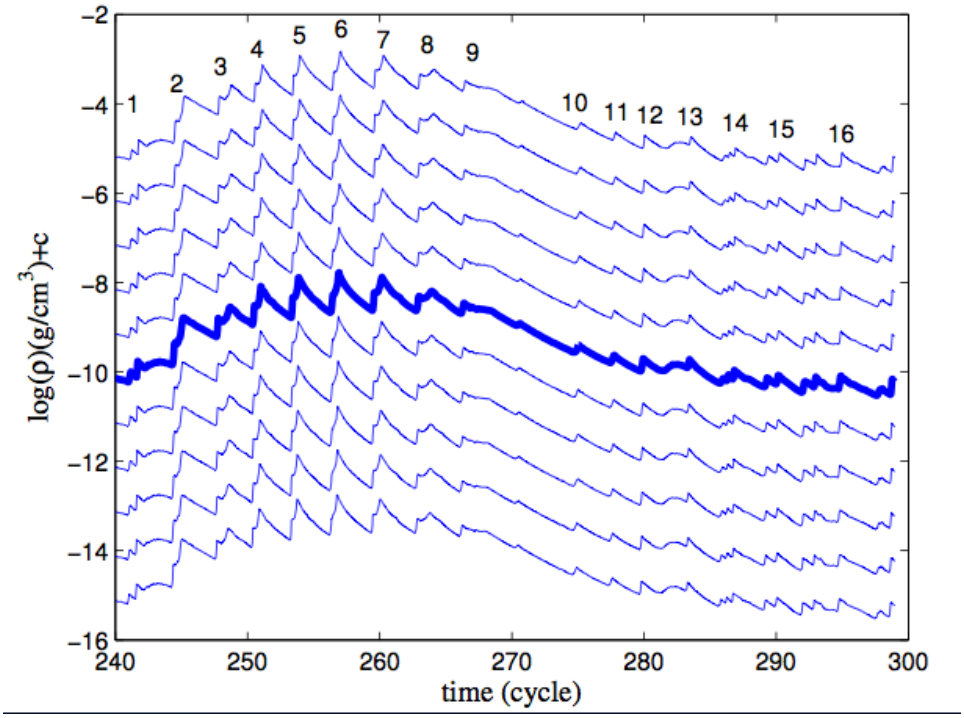

Figure 3.7 Density vs. time for eleven layers of the model 5. The central layer has radius $R = 1.5 \times 10^{14} cm$ and the separation of the layers is $10^{12} cm$. The density curves are offset by an arbitrary constant C = 0 to 10 from bottom to top. The shock speed can by calculated by tracing the density peaks across the $10^{13} cm$ displayed here. All numbers are listed in Table 3.3.

Comparing the number of gaps, the faster spiral arms may also show more windings. This is demonstrated in Figure 3.10 showing slices of the atmosphere at cycle 600 for Models 3 - 6. The time is chosen to make sure that spiral arms are clear in that slice. The vertical offset is artificial in order to separate different series. In this figure, the lowest curve for Model 3 $M_{comp} = 5 M_{Jupiter}$ keeps its real value. The separation between curves is $\Delta log(\rho) = 1$. The average properties of each segment are listed in Figure 3.4.

Each spiral arm is a combination of two groups. The rear group shows a dominating strength early on. It is the group of fast-moving strong shocks in Figure 3.9. The front group is the decelerating weak shocks as described. The front shock is defined as the density drop on the front boundary of a spiral arm. The rear shock is defined as the density drop on the rear boundary. Both of them are shown in detail in Figure 3.10. The density drops on the cliffs of front shocks and rear shocks show similar values between different models. The front shock

Table 3.3 The properties of shocks between cycle 240 - 300 of Model 5

Shocks	Speed(km/s)	$log(\rho)$ (gm/cm^3)	T(cycle)
1	8.813	-14.704	241.6
2	8.813	-13.735	245.4
3	13.219	-13.508	248.6
4	13.219	-13.027	250.9
5	13.219	-12.868	253.8
6	8.813	-12.825	256.9
7	8.813	-12.853	260
8	13.219	-13.158	263.8
9	8.813	-13.389	266.3
10	6.61	-14.348	275
11	13.219	-14.597	277.8
12	13.219	-14.644	280
13	13.219	-14.666	283.5
14	13.219	-14.926	286.9
15	25.44	-15.03	290.2
16	13.219	-15.27	297.6

Table 3.4 The average properties of shocks of models 5, 8, 10, 12

M_{comp} $(M_{Jupiter})$	shock front speed (cm/s)	shock rear speed (cm/s)	shock front $dlog(\rho)(gm/cm^3)$	shock rear $dlog(\rho)(gm/cm^3)$
5	1.26×10^6	1.07×10^6	0.670	0.535
8	1.32×10^6	1.11×10^6	0.668	0.583
10	1.28×10^6	1.13×10^6	0.623	0.498
12	1.33×10^6	1.18×10^6	0.638	0.540

density drop is a little more than a factor of 4 indicating some energy lost to radiation. The density drop for rear shocks is less than 4, appropriate for adiabatic shocks. As the spiral arms move out and grow wider, the difference in density between the two parts starts to disappear around $1 \times 10^{16} cm$. Then the spiral arms begin to overlap with each other after $1.5 \times 10^{16} cm$ for $M_{comp} = 5 M_{Jupiter}$.

Interesting spikes in density appear after the spiral arms combine. This behavior is best illustrated in Figure 3.11, which tracks a very extended atmosphere from Model 5 at a time = 1200 cycles. We set the outer boundary of the simulation to about $4.5 \times 10^{16} cm$ ($\sim$ 3000AU). The spiral arm structures first disappear at $2 \times 10^{16} cm$ due the widening. But after the spiral

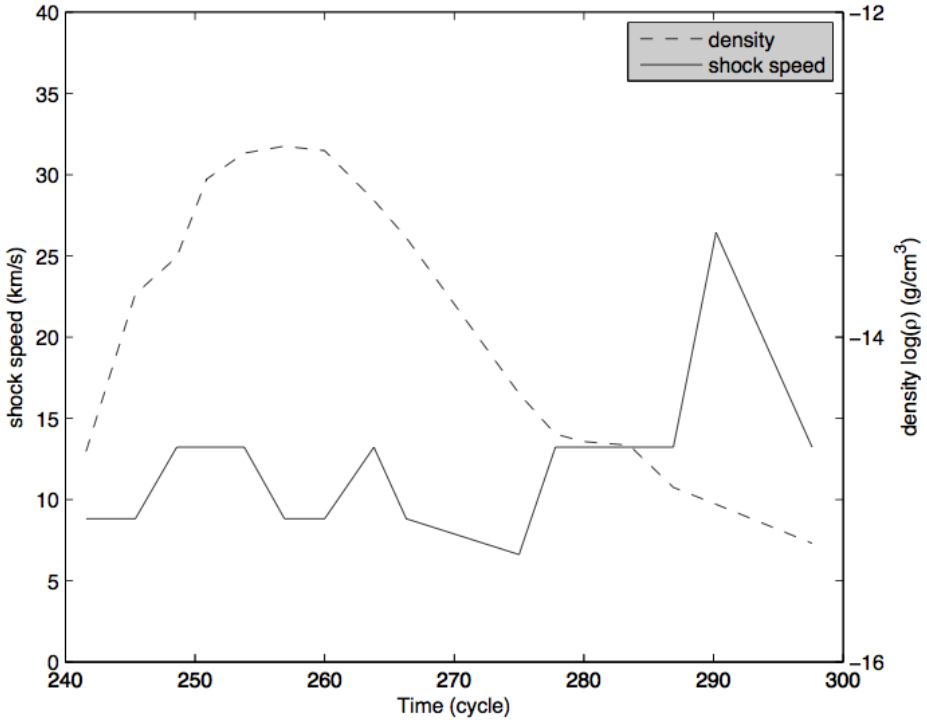

Figure 3.8 Peak density and shock speed vs. cycle number for Model 5. The numbers are listed in Table 3.3. The dotted line gives the density and the solid line, the shock speed computed as illustrated in Figure 3.7. The strong shocks are found before cycle 270 and weaker ones after 270.

arms merge, spikes with the same periodicity begin to develop. These spikes are weak compared to the spiral arms and show the widening around $4 \times 10^{16} cm$ again.

In the following pictures, we construct 2-D images of the outflows in the equatorial plane from the 1-D models. For the whole star, different positions on the surface are always experiencing the same pulsation phase but a different orbital phase of the companion. From the 1-D calculation, we select instances with the same pulsation phase and different orbital phases and distribute these around the center according to orbital phase. This then represents a snapshot of what the equatorial distribution of material may be like in a full 2-D model, noting that we have not allowed the material to interact other than radially in these models. If we have long enough runs and the outflow is stable, we can get enough pieces to create the whole surroundings. But this is limited by the reservoir of material available in the model and the rate of depletion of this reservoir by mass loss. In most runs, we stop the model at 1000 cycles when

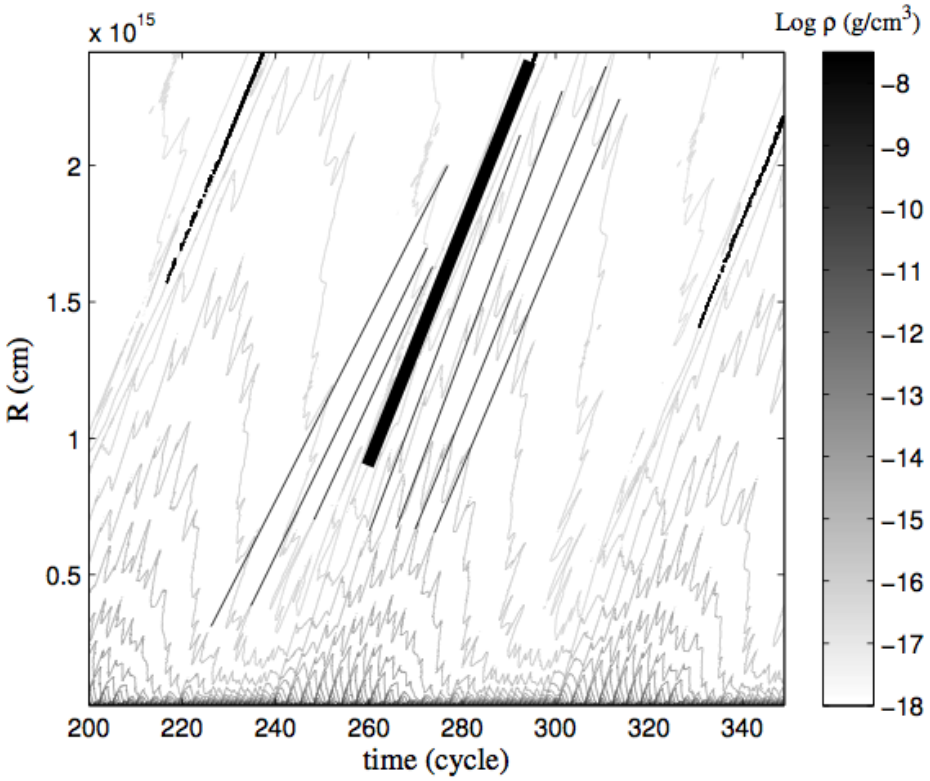

Figure 3.9 This picture traces the positions of mass shells during cycles 200 - 240 with the density coded by the color. The interval shown in Figure 3.5 occurs in the middle of this plot, with more than two spiral arm periods shown here. The straight line segments trace shock trajectories; they converge towards the heavy line. This convergence produces the spiral arms.

the spiral arms are getting faster because the density is lower after mass loss; this leads to two artifacts in the graphs: (a) spikes on the spiral arms in the plot due to higher speed in some phases, (b) the gaps in the graph due to missing some phases.

Models 3 - 6 all produce three spiral arms. Figure 3.12 shows the density color map of the extended outflow of Model 5. In the central region, three spiral arms are clear until they become wide and their density profiles even out at about $2 \times 10^{16} cm$. Then the spiral pattern reappears close to $3 \times 10^{16} cm$ as seen in Figure 3.11. Figure 3.13 is the T_{kin} contour map of the inner region ($< 1 \times 10^{16} cm$). Since non-LTE is assumed for the thin outflow, no accurate spectral information can be derived from T_{kin} alone in this picture; however, molecular formation is sensitive to T_{kin}. The spiral arms may cut through the molecular shell and give it a non-spherical shape perhaps explaining the observation by Ragland et al. (2008). The spikes on the

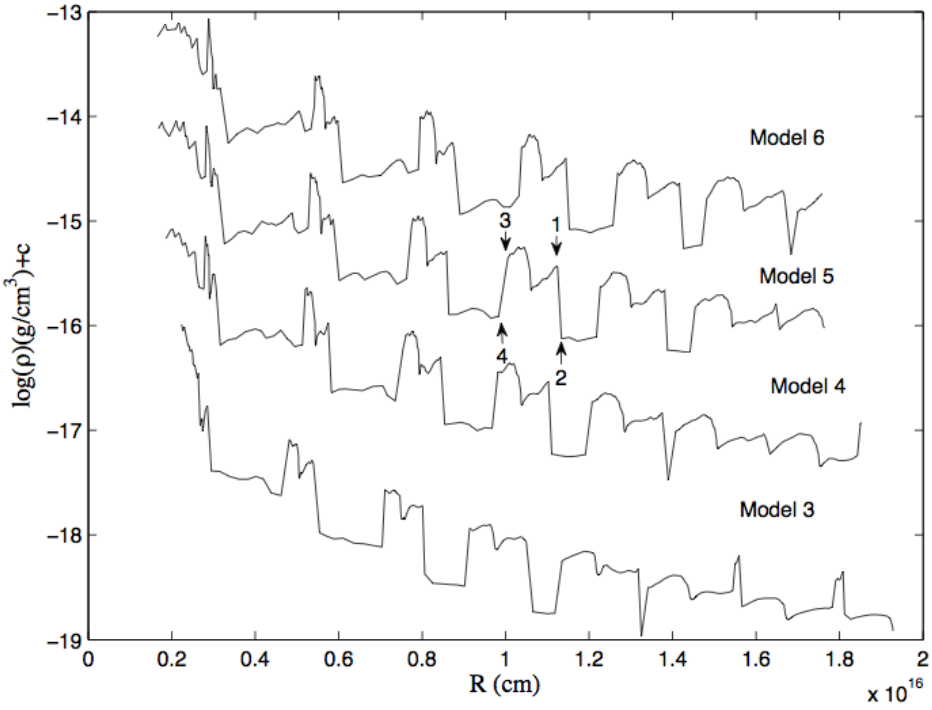

Figure 3.10 Density vs. height at cycle 600 for Models 3-6. The companion mass increases with increasing model numbers. There is an artificial offset of C = 1 to 3 for Models 4-6. The front shock is defined as the density drop between position 1 and 2 indicated on Model 5. The rear shock is defined as the density drop between position 3 and 4. The positions of front shocks and rear shocks are chosen to be the same as positions 2 and 4. The density differences are compared between 1 and 2 , 3 and 4 for different cliffs. Similar analyses are done to all cliffs in all models. Numbers are listed in Table 3.5.

contour are caused by the non-stable atmospheric conditions at the end of the run as discussed above.

Models 1 and 2 have 4 spiral arms. The companions are very close to the stellar surface (see Table 3.2). They may even be inside the photosphere for some of the time. Since the photosphere is defined at optical depth $\tau = 2/3$ for spherical symmetry, a significant amount of mass still resides below the photosphere between the piston and the photosphere in the model. The companion is well above the piston where the artificial boundary is located. Because these companions are very close to the surface, the gravitational effects of the companions are as large as they reasonably can be. Figure 3.14 shows the density color map for Model 1. The spiral arms are wide from the beginning. They start to merge at around $4 \times 10^{15} cm$. The gaps in the

Table 3.5 The detailed properties of shocks of models 5, 8, 10, 12

shocks		1	2	3	4	5
M05	FS(cm)	2.95×10^{15}	5.54×10^{15}	8.06×10^{15}	1.07×10^{16}	1.33×10^{16}
	RS(cm)		4.62×10^{15}	7.04×10^{15}	9.02×10^{15}	1.12×10^{16}
	RS$dlog(\rho)(gm/cm^3)$		0.53	0.55	0.54	0.52
	FS$dlog(\rho)(gm/cm^3)$		0.69	0.64	0.70	0.65
	gap(cm)		1.67×10^{15}	1.50×10^{15}	9.60×10^{14}	5.20×10^{14}
	shock width(cm)		9.22×10^{14}	1.02×10^{15}	1.64×10^{15}	2.07×10^{15}
M05	FS(cm)	3.16×10^{15}	5.83×10^{15}	8.54×10^{15}	1.11×10^{16}	1.39×10^{16}
	RS(cm)		5.13×10^{15}	7.36×10^{15}	9.67×10^{15}	1.19×10^{16}
	RS$dlog(\rho)(gm/cm^3)$		0.54	0.67	0.62	0.50
	FS$dlog(\rho)(gm/cm^3)$		0.67	0.65	0.70	0.65
	gap(cm)		1.97×10^{15}	1.53×10^{15}	1.13×10^{15}	8.10×10^{14}
	shock width(cm)		6.94×10^{14}	1.18×10^{15}	1.43×10^{15}	1.99×10^{15}
M05	FS(cm)	3.26×10^{15}	6.01×10^{15}	8.58×10^{15}	1.13×10^{16}	1.39×10^{16}
	RS(cm)		5.27×10^{15}	7.62×10^{15}	9.83×10^{15}	1.22×10^{16}
	RS$dlog(\rho)(gm/cm^3)$		0.52	0.50	0.49	0.48
	FS$dlog(\rho)(gm/cm^3)$		0.63	0.60	0.69	0.57
	gap(cm)		2.01×10^{15}	1.61×10^{15}	1.25×10^{15}	8.40×10^{14}
	shock width(cm)		7.40×10^{14}	9.60×10^{15}	1.51×10^{15}	1.70×10^{15}
M05	FS(cm)	3.35×10^{15}	6.10×10^{15}	8.90×10^{15}	1.15×10^{16}	1.43×10^{16}
	RS(cm)		5.34×10^{15}	7.91×10^{15}	1.03×10^{16}	1.26×10^{16}
	RS$dlog(\rho)(gm/cm^3)$		0.50	0.57	0.59	0.50
	FS$dlog(\rho)(gm/cm^3)$		0.59	0.69	0.64	0.63
	gap(cm)		1.98×10^{15}	1.81×10^{15}	1.42×10^{15}	1.05×10^{15}
	shock width(cm)		7.59×10^{14}	9.95×10^{14}	1.20×10^{15}	1.69×10^{15}

radial direction are artifacts due to limited running time; similar patterns are common among these models. On the density profile in Figure 3.15, the lowest mass companion produces very poor density contrast between the spiral arm and inter-arm region. The clustering of the shocks looks chaotic. The density profile only shows the merging spikes after spiral arms converge. This model has the weakest spiral arms for the model in the closest orbit. Since the star in Model 1 is already losing mass fast ($\sim 10^{-6} M_{\odot}/yr$), any companion with a mass smaller than 2 $M_{Jupiter}$ is not expected to produce strong spiral arm patterns.

Figure 3.16 for Model 2 is similar to Figure 3.14 but with an increasing companion mass from 2 $M_{Jupiter}$ to 5 $M_{Jupiter}$. The spiral arms of Model 2 are prominent according to the density profile at cycle = 900 in Figure 3.17, but the four spiral arms are not very clear due

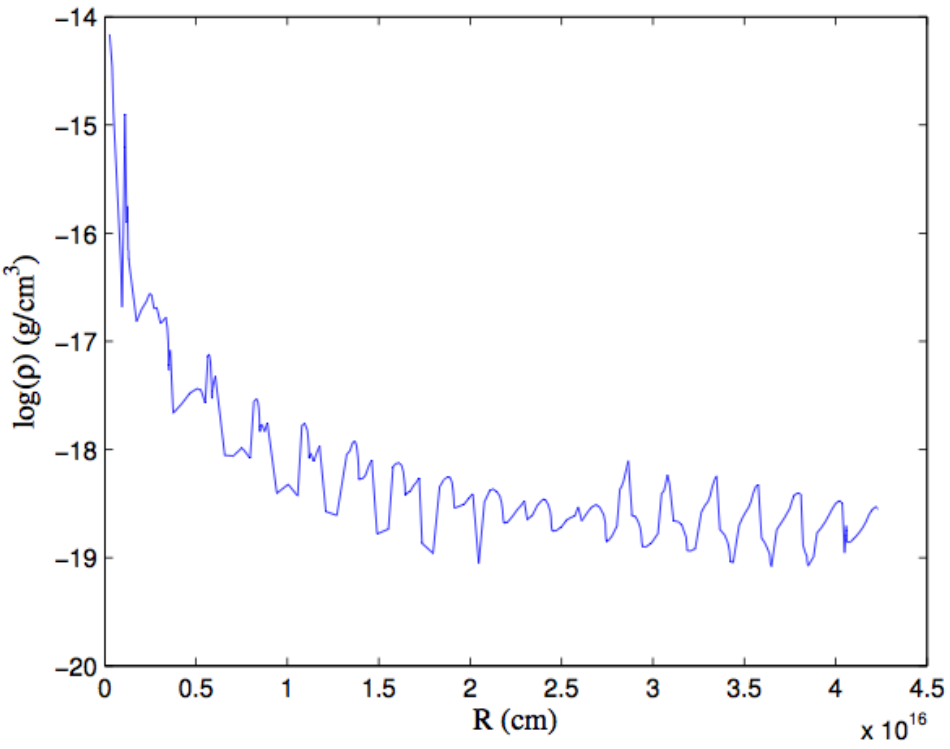

Figure 3.11 Density vs. height for Model 5 extending to $R = 4.5 \times 10^{16} cm$, showing the spike structure that forms after spiral arms merge.

to artificial spikes. This indicates that the atmospheric conditions changes quickly during the run. The $5M_{Jupiter}$ companion causes greater mass loss and makes the atmosphere thinner than that a more stable model would require.

Models 7 and 8 show 2 spiral arms. The companions are relatively far away compared to the previous models. Because the orbital periods for these two models are different, they have different spiral arm periods. Comparing Figures 3.18 and 3.20, we see that the short spiral arm period gives more windings within the same distance. In Figure 3.19, the density profile for Model 7 shows similar spiral structures compared to the previous short P_{sa} models. For the long spiral arm period picture in Figure 3.20, the clustering is not established within the region calculated, but the bipolar structure is similar to the central region in the density color map in Figure 3.18. The slow clustering is also reflected in the density profile in Figure 3.21. The two bumps represent the rear shock and front shock. They have not become narrow yet, so no steep density drop exists on the edges.

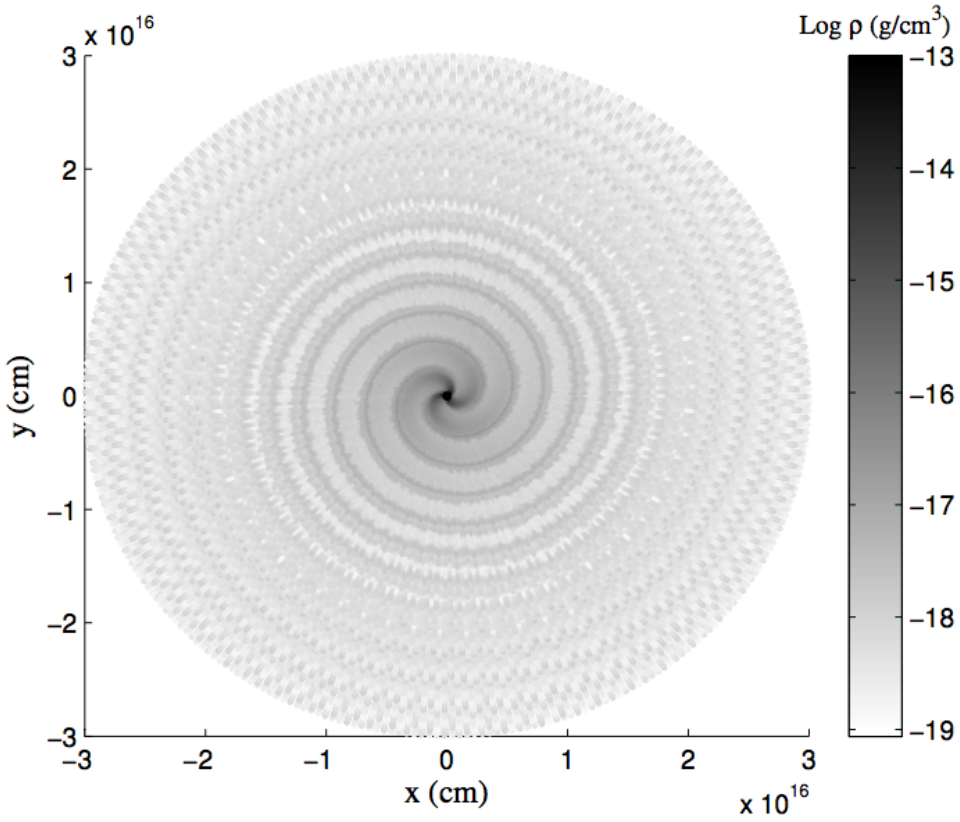

Figure 3.12 Density vs. position in the equatorial plane for Model 5, constructed from the 1D model as described in the text.

In Model 9, the spiral arm period is the same as the orbital period. In previous models, since the orbital period is smaller than the spiral arm period, multiple shocks are created during one spiral arm period. In that case, it is possible for the clustering to occur that strengthens the density contrast. Model 9 does not show the clustering of multiple shocks. The spiral arm is a single shock created by the companion while it moves through the outflow. Since the disturbance by the companion in the atmosphere is small, it does not enhance the mass loss much. In Figure 3.22, unlike in previous models there is no spike at the location of spiral arms. In Figure 3.23, the density profile shows almost no difference at the spiral arm location. Model 9 matches periodicity of the recent observations of a single-spiral outflow (Mauron & Huggins, 2006) but with a very low contrast. To get something more like what is observed, one would need a higher mass companion, and would then need to consider distortion of the star and tidal spin-up, neither of which are included in our code.

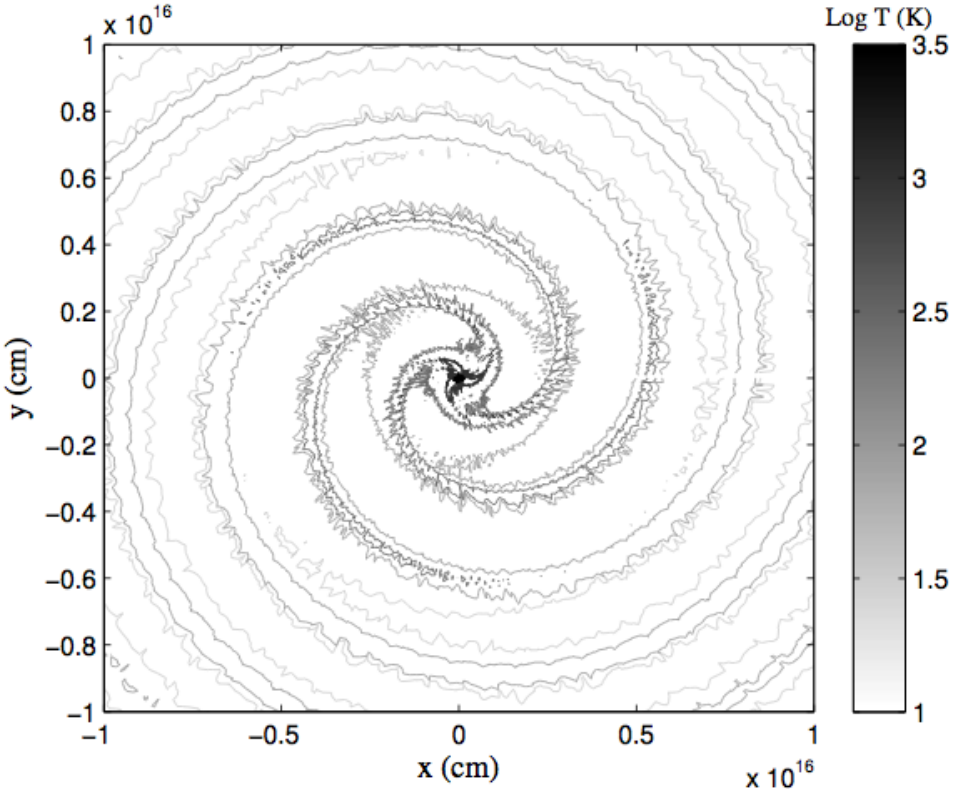

Figure 3.13 Contour map of the gas kinetic temperature for Model 5. T_{kin} is affected by both the shocks (expansion, compression) and the radiation field. Due to the treatment of non-LTE in the code, T_{kin} does *not* translate easily into intensity of emission.

3.4 Discussion

3.4.1 Spiral arm period

From the models and some analytic considerations, we have found the following formula relating to resonance of the pulsation and orbital period (Struck, private communication):

For N > 1,

$$P_{sa} = \frac{P_{puls} P_{orb}}{|N P_{orb} - M P_{puls}|}, M = 1, \ldots, N-1 \tag{3.3}$$

For N = 1,

$$P_{sa} = P_{orb} \tag{3.4}$$

where P_{sa} is the spiral arm period, P_{orb} is the orbital period, P_{puls} is the pulsation period, and N is the number of spiral arms, M is the resonance mode. To understand the origin of

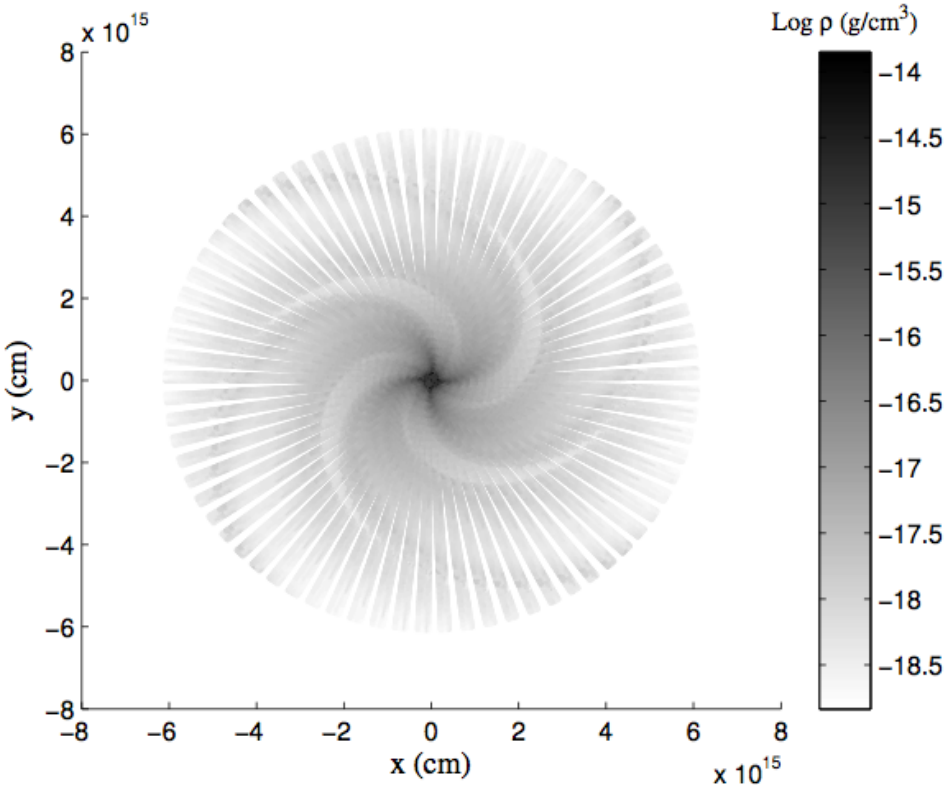

Figure 3.14 Density vs. position in the equatorial plane for Model 1. The dark spiral arms are wide and catch up with each other at around $4 \times 10^{15} cm$. The radial gaps are artifacts of the method we used to construct the map.

this expression, consider what happens in Model 5. The companion will encounter the same phase of the pulsation after intervals of $P_{puls}/P_{orb} \sim 2/3$ of its orbital phase. If a strong shock is generated at phase 0, then this will happen again at 2/3 and 4/3 (= 1/3 in the next orbit). So the difference in orbital phase between nearest strong shocks is 1/3. Three arms are seen around the star in the equatorial plane. When N is 1, P_{sa} equals to P_{orb}. This is the same relation as shown in Model 9. In Figure 3.24, we plot the relation between P_{sa}/P_{puls} and P_{orb}/P_{puls} from Eqns. 3.3 and 3.4 for several values of N. For resonance mode, we choose M = N -1. These resonance modes have closer orbits than M<N-1, which means stronger influence by the companion. Since we can not determine the distance at which the companion influence is negligible, we choose only the close orbit companions. The large orbit resonance modes are omitted in the following discussion. We did not model N = 5 in this paper either because the companion falls inside the photosphere. Figure 3.24 reveals that it is very hard

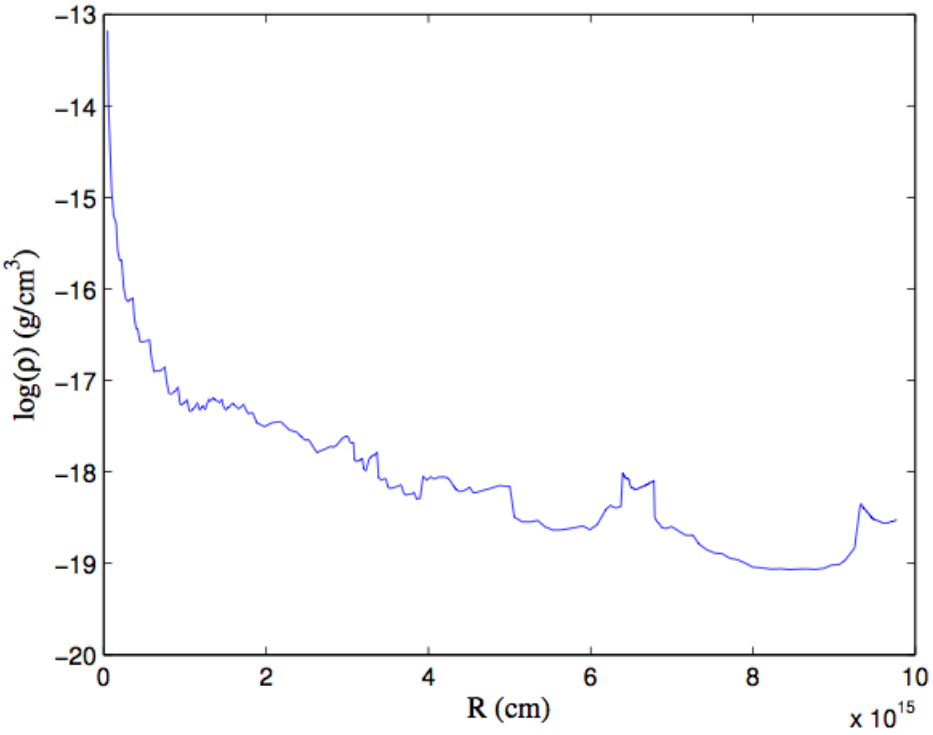

Figure 3.15 Density vs. height for Model 1 at cycle 900. The spiral arms in this case merge near $4 \times 10^{15} cm$. The spikes above $6 \times 10^{15} cm$ are not the results of clustered spiral arms.

to get over $P_{sa}/P_{puls} = 100$. It is also hard to drop below $P_{sa}/P_{puls} = 10$ in the near orbit ($P_{orb} < 2.2 P_{puls}$). Since one can relate P_{orb} to the orbital radius, only close companions are capable of generating multiple spiral arms. Any system with $P_{orb} > 3P_{puls}$ is going to have a single dominant spiral arm.

When the radius of a late type star increases, its fundamental pulsation period increases as well, while the orbital period of the companion remains the same. So for a close companion (e.g. the Jupiter in our solar system), P_{orb}/P_{puls} will eventually match multiple spiral arm relations as the central star grows bigger and bigger at the end of its AGB evolution. We estimate the duration of the effective interaction as below. We examine the evolution of $X = P_{orb}/P_{puls}$ as a result of mass loss, tidal drag and gas drag on the planet. The angular momentum of the planet in orbit for $M_{comp} \ll M_{star}$ is $L = M_{comp} v_{comp} r_{orb}$ with $v_{comp} = (GM_{star}/r_{orb})^{-1/2}$ for a circular orbit, so we get

$$r_{orb} = (GM_{comp}^2)^{-1} L^2 / M_{star}, \tag{3.5}$$

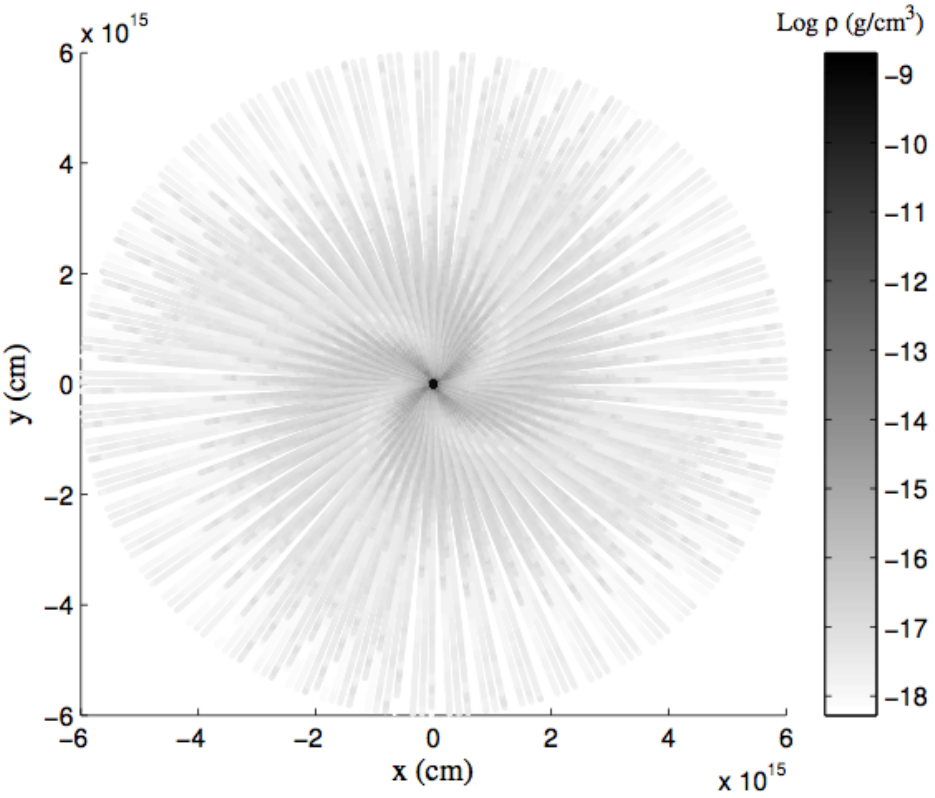

Figure 3.16 Density map for Model 2. The spiral arms are tighter than for model 1 and do not merge inside of $6 \times 10^{15} cm$.

where M_{star} is the mass of the star, r_{orb} is the orbital radius of the companion, M_{comp} is the mass of the companion, v_{comp} is the velocity of the companion and L is its the angular momentum. We can combine Eqn. 3.5 with Kepler's third law to get

$$P_{orb} = 2\pi G^{-2} M_{comp}^{-3} M_{star}^{-2} L^3. \tag{3.6}$$

All quantities in Eqn. 3.6 are in cgs units. The pulsation period for fundamental mode P_{puls} (Ostlie & Cox, 1986) is

$$P_{puls} = 0.012 M_{star}^{-0.73} R_{star}^{1.86}, \tag{3.7}$$

where P_{puls} is in days, M_{star} and R_{star} are in solar units. The ratio of P_{orb} and P_{puls} controls the spiral arm period and is

$$X = \frac{P_{orb}}{P_{puls}} = 166.7 C \pi G^{-2} M_{comp}^{-3} M_{star}^{-1.27} R_{star}^{-1.86} L^3. \tag{3.8}$$

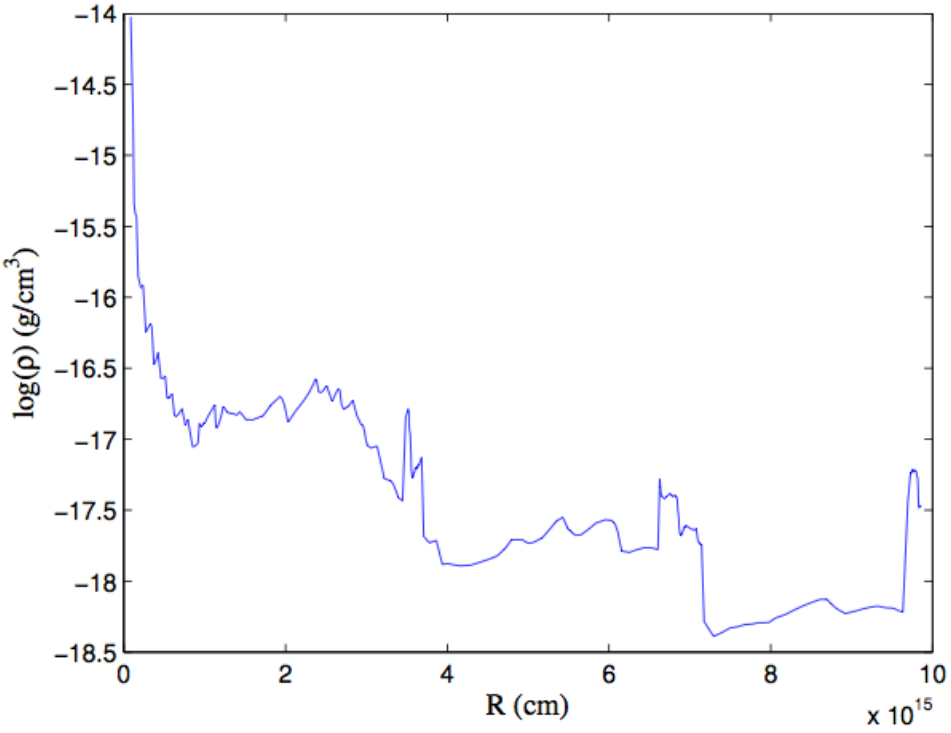

Figure 3.17 Density profile of the atmosphere of Model 2 at cycle 900 showing strong density contrast for the spiral arms located at about $3.5\times10^{15}cm$, $7\times10^{15}cm$ and $10^{16}cm$.

Since the units in Eqns. 3.6 and 3.7 are different, we introduced C to balance the equation; it is canceled in Eqn. 3.9. The rate of evolution of lnX, the inverse of the characteristic e-folding time, in terms of evolution of M, R and orbital angular momentum L is

$$\frac{1}{X}\frac{dX}{dt} = \frac{\dot{X}}{X} = -1.27\frac{\dot{M}_{star}}{M_{star}} - 1.86\frac{\dot{R}_{star}}{R_{star}} + 3\frac{\dot{L}}{L}. \tag{3.9}$$

The radius of the star changes for two reasons: the mass loss of the star

$$\frac{\dot{R}_{star}}{R_{star}} = -0.2\frac{\dot{M}_{star}}{M_{star}} \tag{3.10}$$

and the nuclear evolution of the star

$$\frac{\dot{R}_{star}}{R_{star}} = 2\times10^{-7}yr^{-1}. \tag{3.11}$$

These results are from our evolutionary models. Substituting Eqns. 3.10 and 3.11 into Eqn. 3.9, we get

$$\frac{\dot{X}}{X} = -0.898\frac{\dot{M}_{star}}{M_{star}} + 3\frac{\dot{L}}{L} - 3.72\times10^{-7}yr^{-1}. \tag{3.12}$$

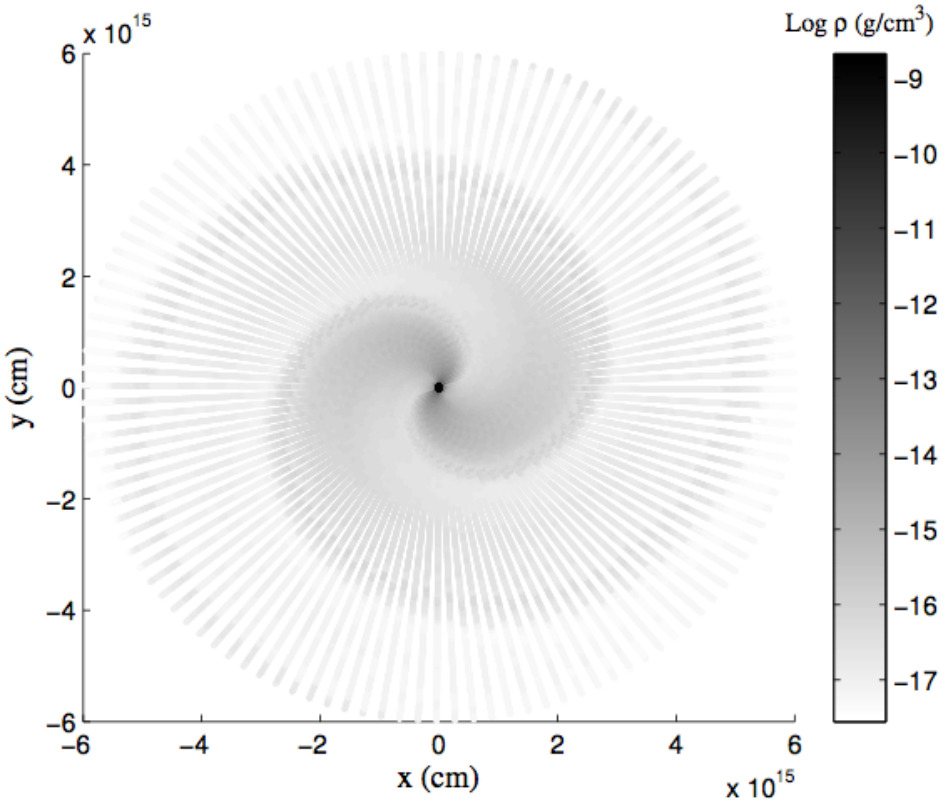

Figure 3.18 Spiral density map for Model 7.

Using the dynamical models, we can estimate the angular momentum evolution $\dot{L}/L$ from two processes - gas drag and tidal drag. For model 5, the mass loss rate is $\dot{M}_{star}/M_{star} = -1.27 \times 10^{-6}/yr$. Gas drag is given by

$$F_{drag} = 1/2\rho_{gas}v^2{}_{comp}C_dA, \tag{3.13}$$

where ρ_{gas} is the gas density, v_{comp} is the velocity of the companion, $C_d = 1.0$ is the drag coefficient for a sphere moving super sonically, and A is the cross-section of the companion.

To estimate the effect of the gas drag on the change of angular momentum, we take the numbers from Model 5 and average the drag force over 60 cycles (1 spiral arm period). The change in angular momentum $\dot{L}/L$ from gas drag for Model 5 is $-2.6 \times 0^{-6}yr^{-1}$. We estimate the tidal drag by summing all gravitational attractions from all zones in Model 5 averaged over 60 cycles. Since the mass of the companion is low, the deformation of the surface is local. Since the 1-D model does not provide enough spatial information to calculate the gravitational attraction, we assume that the companion affects an area of approximately its own size at the

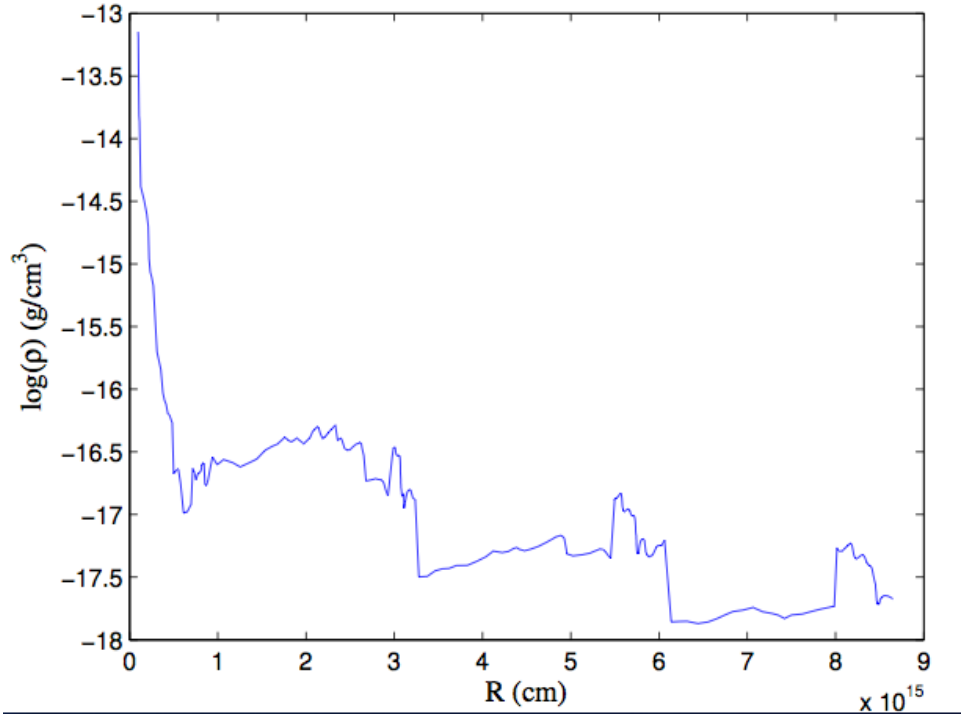

Figure 3.19 Density profile of the atmosphere of Model 7 at cycle 900. It shows good density contrast for the spiral arms located at about $3 \times 10^{15} cm$, $6 \times 10^{15} cm$ and $8.5 \times 10^{16} cm$.

photosphere. We then assume that the area increases as the radius of the zone increases, keeping a fixed solid angle. With the width and density of the zones from our 1-D model and the areas of the zones, we can calculate the gravitational pulling from each zone to the companion. Due to the shear force between the disturbed and normal outflows, the disturbed outflows may not be able to travel as far as predicted in our 1-D model, so the tidal drag calculated here is probably an upper limit. The change in angular momentum $\dot{L}/L$ from tidal drag is $-3.44 \times 10^{-5} yr^{-1}$. Thus the overall rate of change expected for Model 5 is $\frac{\dot{X}}{X} = -1.1 \times 10^{-4} yr^{-1}$. For P_{sa}/P_{puls} changing from 10 - 100 in Model 5, the change in the ratio of P_{orb}/P_{puls} is about 4%, and we expect that the decadal pattern will persist for about 400 years. To get constant X, one would require a mass loss rate of $\dot{M}_{star} = -1.2 \times 10^{-4} M_{star}/yr$ (possibly more since the tidal and gas drag would also increase). For mass loss rate of these models, we would expect the system to evolve away from the condition that produces well-separated spiral arms on a timescale of a few hundred years. Figure 3.25 is a demonstration of a companion with orbital decay time

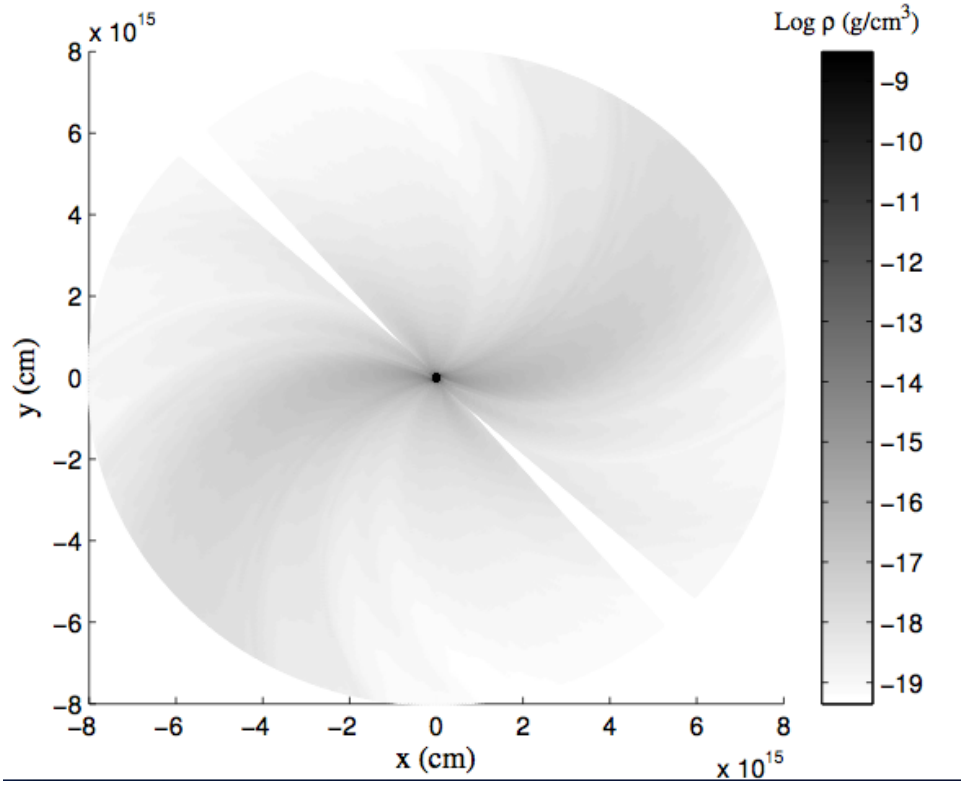

Figure 3.20 Spiral density map for Model 8. While spiral arm stays broad to the edge of the graph, the central region is similar to that of Figure 3.18.

scale of 10^4 using a simplified relation based on Eqn. 3.3.

A similar analysis for $Y = r_{orb}/R_{star}$ yields,

$$\frac{\dot{Y}}{Y} = 1.2\frac{\dot{M}_{star}}{M_{star}} + 2\frac{\dot{L}}{L} - 2 \times 10^{-7} yr^{-1}. \tag{3.14}$$

For model 5, $\frac{\dot{Y}}{Y}$ is $-7.3 \times 10^{-5} yr^{-1}$. We can visualize the change in the companion orbit with this time scale. To maintain a fixed Y, the mass loss rate would need to be more than $\dot{M_{star}} = -5 \times 10^{-5} M_{star}/yr$. Since the companion orbital radius in Model 5 is approximately median among all models, we expect a fast decay of orbital radius for a closer companion and a slower decay for a farther companion. Because it is difficult to get $\frac{\dot{Y}}{Y}$ and $\frac{\dot{X}}{X}$ to be 0, we conclude that a stable long term structure is unlikely to occur. These planets will spiral in on a time scale of 10^4 to 10^5 years. For comparison, the "superwind" phase of a solar AGB star lasts 2×10^5 years.

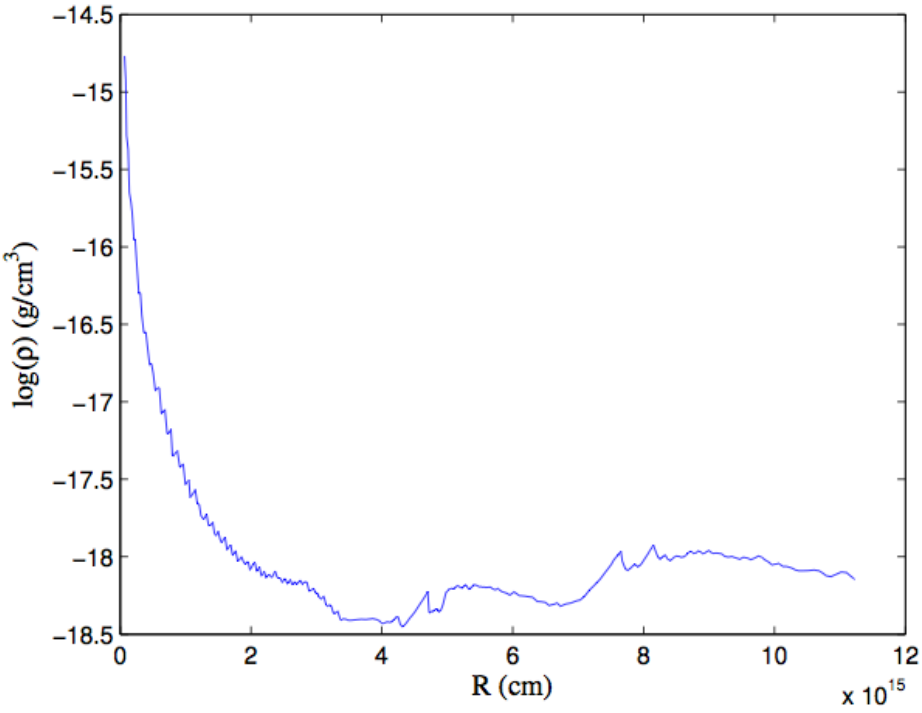

Figure 3.21 Density profile of Model 8 at cycle 900, showing one wide spiral arm near $R = 8 \times 10^{15} cm$.

3.4.2 Observational considerations

These models suggest that some interesting outflows, including three-armed spirals, may occur when a large planet is close to a pulsating, mass-losing star. In this section, we consider how such spirals may be observed. In what follows, the reader should keep in mind that the present models are 1-dimensional, and thus do not include bow shocks, the horizontal interactions between the planet and the atmosphere features, and the freedom that a 2-D or 3-D structure has to spread out in these additional dimensions. Thus, the estimates are at best order-of-magnitude.

A comparison between the column density along the central plane and through the unperturbed wind the rest of the outflow is presented in Figure 3.26 for a pole-on view. The unperturbed outflow is the outflow without the companion and is uniform in all directions. The distances from the lines of sights to the central star range from 2 - 150 R_{star}. To estimate the column density in the central plane, we assume the outflow starts with the size of

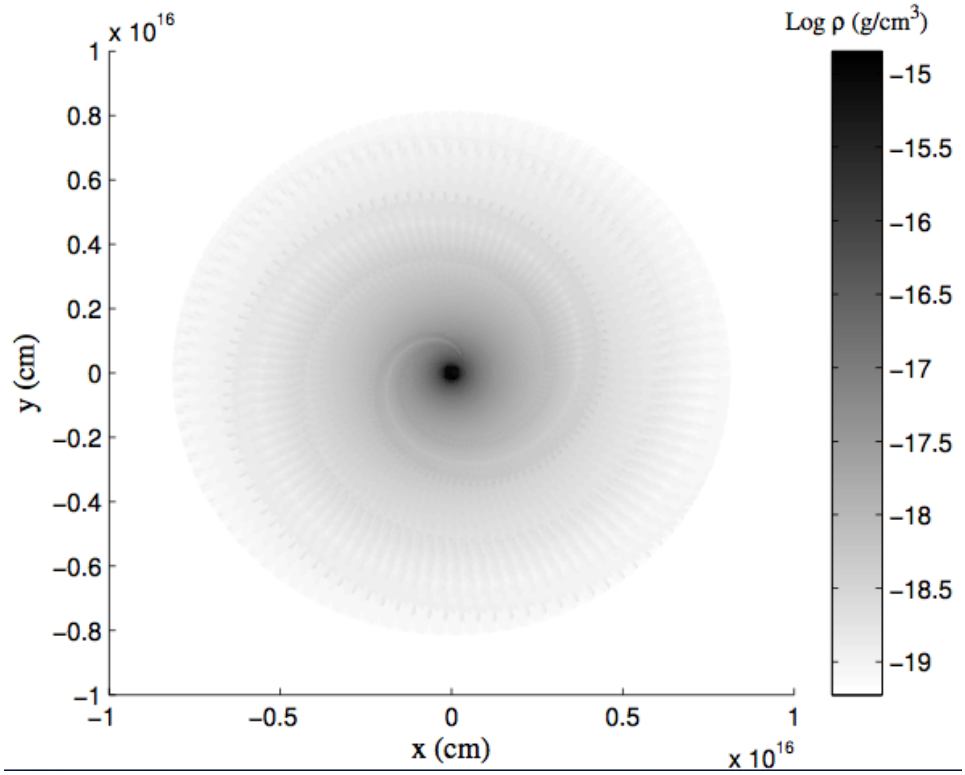

Figure 3.22 Density map for Model 9. We expect the smooth spiral arms where the atmosphere does not lose mass to fast and maintain a steady outflow.

the companion on the photosphere and grows larger with a fixed solid angle; it is a thin disk with a thicker edge. With this assumption, we calculate the column densities at different lines of sights. The lines of sight for central disk cover the same range as the normal flow does, perpendicular to the central plane. At 2 R_{star}, the normal outflow column density is more than 2.5 orders of magnitude larger than the central plane column density. The central plane column density goes further down in the post spiral arm region. At about $150R_{star}$, where shocks cluster into spiral arms, the column density in the undisturbed outflow is only a little over 1 order of magnitude higher than that of the developing spiral arm in the central disk. Considering that the width of the central plane at $150R_{star}$ is only ~ 0.15 R_{star}, the density increase is quite significant in the equatorial plane. The spiral arm may still be weak, if we observe from above; the optical depth along the equatorial plane is much larger. However, with an edge-on view we will not be able to determine the number of spiral arms.

From Figure 3.24, we can see that the structure of multiple arms is very sensitive to the

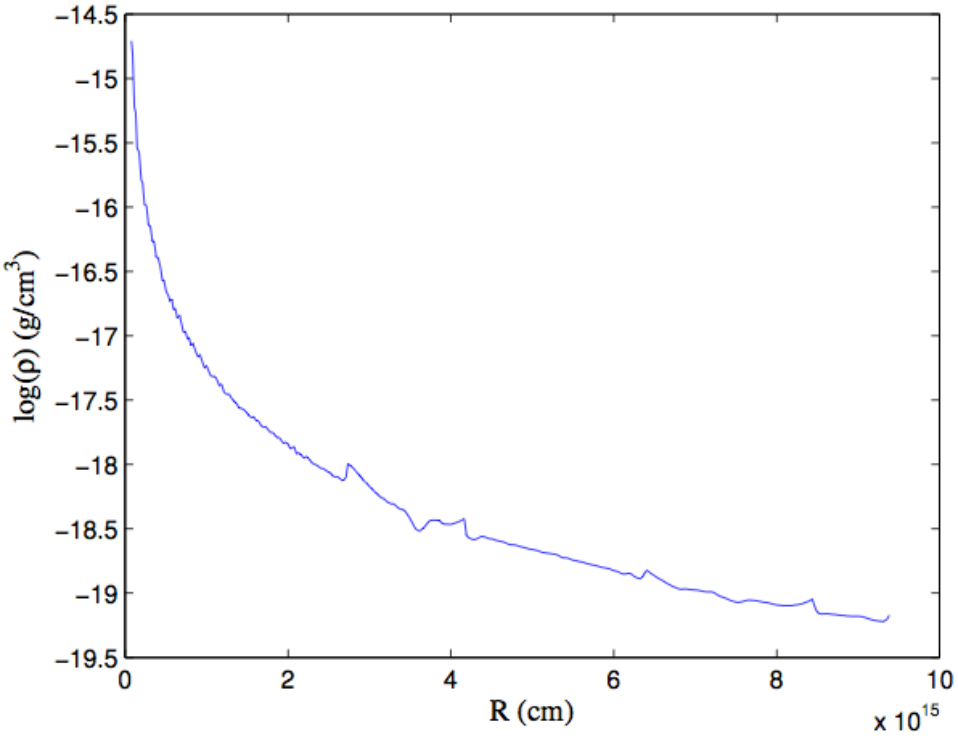

Figure 3.23 Density profile for Model 9 at cycle 900, showing weak contrast in the spiral arms located near $R = 4 \times 10^{15} cm$ and $R = 8 \times 10^{15} cm$.

orbital radius. Small orbital changes may result in large changes in the spiral arm period. The variation in time scales matches the result of IRC-10216 (Mauron & Huggins, 1999, 2000). If this is the case, the spiral arms in IRC-10216 are broken into many segments with different time scales ranging from smallest near the star to longest far out. Simis et al. (2001) also produced the quasi-periodic shells models matching the varying time scale.

We would not expect to see very many late AGB stars with close super-Jupiter companions at any moment, because the duration of this phase is short. A recent discovery that may be relevant is that of material around LL Pegasi (Mauron & Huggins, 2006), but the large contrast and single spiral structure suggest higher companion masses than we are considering here, as was confirmed by Morris et al. (2006). The models of Mauron & Huggins (1999) may be more appropriate to that case.

The full spiral structure may not be developed since the spiral arm time scale may be longer than the stable orbit time scale. But if we can resolve the very inner region, multipolar outflow

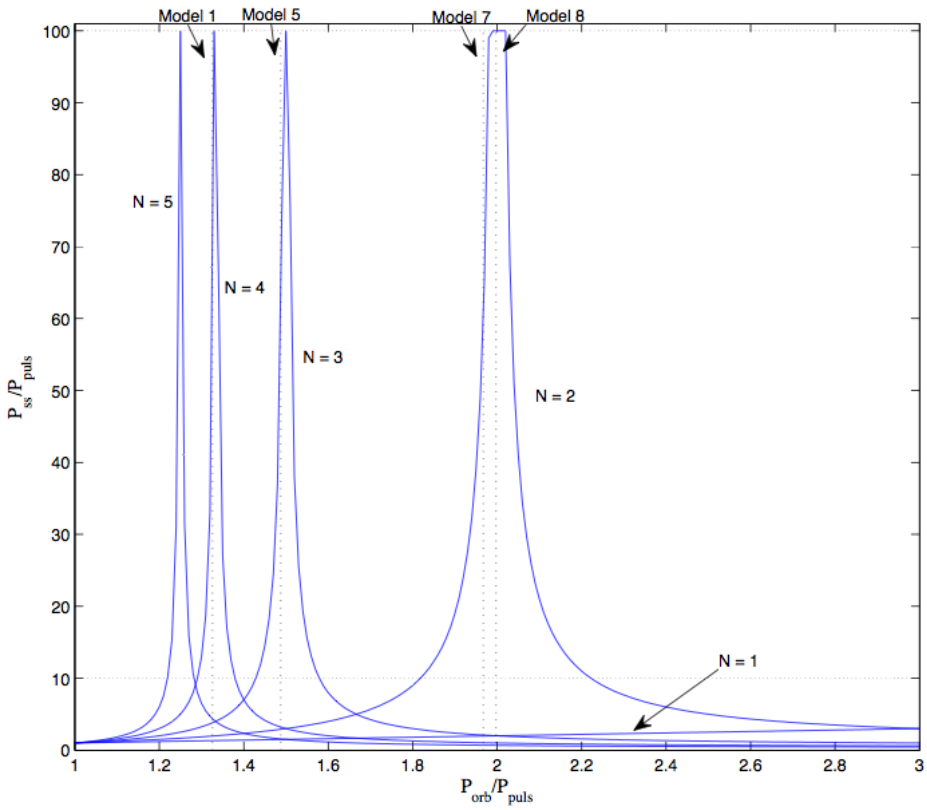

Figure 3.24 Spiral arm period as a function of orbital period from Eqn. 3.3. The vertical dashed lines indicate the periods of Models 1, 5 ,7 and 8. One dotted line is placed at $P_{sa}/P_{puls} = 10$ to show the results with $P_{sa}/P_{puls} > 10$. N is the number of spiral arms for a given spiral arm period. Line N=1 is close to the bottom and intersects with line N = 2 at $P_{sa}/P_{puls} = 3$.

may be detectable with timescales of hundreds of years. A tripolar enhancement (Figure 3.25)in the outflow is unique to our models.

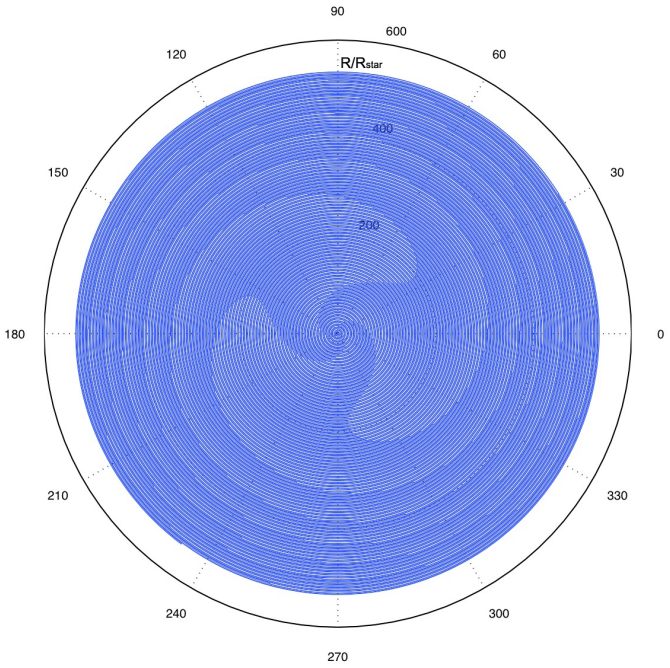

Figure 3.25 Companion on a decay orbit. The orbital period is in the vicinity of the Model 5. The decay time scale of the orbital period is 10^4 years. The turn in the shape of spiral is caused by crossing the resonance maximum at $NP_{orb} = MP_{puls}$. This is plotted using a simplified equation based on Eqn. 3.3 not from actual model calculations.

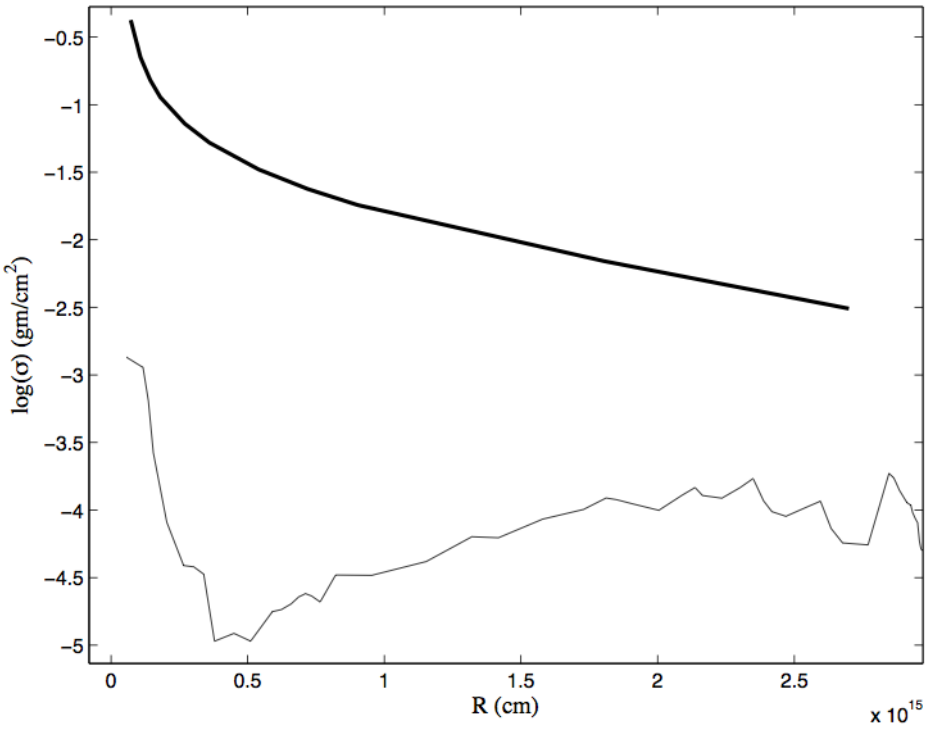

Figure 3.26 Column densities in the central plane (thin line), estimated as described in the text, compared with the column density in the unperturbed wind (thick line). Column density alone is not likely to make the spiral arms visible in this example, but they may become visible if the opacity coefficient is higher in the central disk (for example in molecular lines or in the UV).

CHAPTER 4. Conclusions and Future perspectives

In this chapter, I discuss the interpretations and limits of the models in Chapter 3. Some future perspectives are also presented . Since the Bowen code is constructed using a Lagrangian grid; it is limited to 1-D calculation. In order to simulate the outflow in 3-D, an Eulerian grid will be needed. I present the equations for calculations using an Eulerian code with 2 fluid dust treatment. Some applications are discussed at the end.

4.1 Conclusions

We have shown that multiple spiral arms can result from the interaction of a low-mass, low-altitude companion with a pulsating, mass-losing AGB star. The most striking and unique result is the possibility of 2, 3 and 4-armed spirals for such close companions. A simple formula relates the spacing of features (via period of spiral arms and the outflow velocity) to the number of spiral arms and the ratio of the orbital period to the pulsation period.

The spiral arms develop a high contrast in gas density as a result of the clustering of shocks with different speeds. The companion passes different parts of the surface at different pulsation phases as it orbits the star. The gravity of the companion couples with pulsation of the star to create shocks of different speeds. In the outer region, the dust and molecules absorb radiation and transfer momentum to the outflows. Finally, these shocks catch up with each other to form periodic spiral arms. This seems to mix two things : (a) this mechanism leads to spiral arm spacing corresponding to a wide range of time scales. (b) However, the orbit of the companion orbit may also be evolving quickly if the star is losing mass fast that the spiral arm structure will typically be incomplete. Close to the star, multipolar outflows should be observable with enhancement in certain directions.

At this stage, these models are only valid for low mass companions, $M_{comp} \ll M_{star}$. Deformation of the star by the companion will add complexity to the dynamics. The simple numerical relation relies on a stable pulsation period. The spherically symmetric condition of 1-D models ignores the shear between the normal outflow and spiral arms, which weaken faster than presented in the model. An enhancement in the equatorial plane with multipolar structure is a general prediction.

4.2 Basic equations for AGB atmosphere modeling

There are two basic types of modeling: Lagrangian and Eulerian zoning. In Lagrangian zoning, the mass inside each grid is fixed. There is no mass transfer between grid cells during the calculation, and only changes of grid size. In Eulerian zoning, the grid is fixed and mass can move between grids. So it is easier to trace the non-LTE properties without the mixing of material in Lagrangian code than in Eulerian code. This makes Lagrangian code more popular. But there are a couple of advantages of Eulerian codes: (1) they have well defined boundaries. (2) Only Eulerian codes allow turbulent flow and arbitrary deformations. The newly developed adaptive mesh codes from Eulerian zoning have the flexibility to adjust locally when conditions change. It's proven to be a better way than Lagrangian zoning in 2-D and 3-D simulations. In 1-D coding, Lagrangian and Eulerian codes are both useful. The Bowen code is still suitable for the purpose of treating mass loss. If one wants to get to higher dimension, Eulerian zoning is OK. In the next section, Eulerian radiative hydrodynamic equations in preparation for a new generation of modeling are presented. One can remove the terms governing the flow between grids and add in the equations for grid sizes to get the equations for Lagrangian zoning.

There are 3 classes for treating dust and gas in the outflow. Gilman (1972) showed that on the stellar surface where density is high enough, dust and gas are both position and momentum coupled. Thus the combination of the two can be treated as a single fluid. But in cool star environments, the density varies quickly, and the condition is not met through out a large area, so it is not always ideal to apply single fluid model. The second class assumes that there is always an equilibrium between the gas drag and the radiation pressure on the dust. The dust moves at its drift velocity without strict position coupling, so the dust speed is the gas

speed plus the drift velocity. The third class makes no assumption about the dust velocity and position. Everything is determined dynamically. So it is a more general treatment and good for more complicated situations. Potentially, one can treat each dust grain size as a fluid, but this is numerically impossible. The equation set here assumes two fluid models.

The equations describing the physics in the model are:

(1), equations of continuity (mass conservation):

$$\frac{\partial \rho_g}{\partial t} + \nabla \cdot (\rho_g v_g) = -S_d \tag{4.1}$$

$$\frac{\partial \rho_d}{\partial t} + \nabla \cdot (\rho_d v_d) = S_d \tag{4.2}$$

S_d is the dust source function indicating the dust generated per unit volume in the gas. It's treated in the dust formation section.

(2), equations of motion (momentum conservation):

$$\frac{\partial}{\partial t}(\rho_g v_g) + \nabla \cdot (\rho_g v_g^2) = \nabla P + H\kappa_g \rho + f_{drag,g} - f_{grav,g} - v_g S_d \tag{4.3}$$

$$\frac{\partial}{\partial t}(\rho_d v_d) + \nabla \cdot (\rho_d v_d^2) = H\kappa_d \rho + f_{drag,d} - f_{grav,d} - v_d S_d \tag{4.4}$$

The drag forces on gas and dust are action and reaction. They are the same in amplitude and proportional to collision rate between dust and gas particles. $f_{drag,d} = -f_{drag,g} = A_d n_g n_d \mu m_H v_D |v_D|$. μ is the mean molecule weight. v_D is the drift velocity. κ_d and κ_g are dust and gas opacities. There is dust pressure.

(3) equations of internal energy (energy conservation):

$$\frac{\partial}{\partial t}(\rho_g e_g) + \nabla \cdot (\rho_g e_g v_g) = -P\nabla \cdot v + 4\pi\rho(\kappa_{g,J} - \kappa_{g,S} S_g) \tag{4.5}$$

$$\frac{\partial}{\partial t}(\rho_d v_d) + \nabla \cdot (\rho_d e_d v_d) = 4\pi\rho(\kappa_{d,J} - \kappa_{d,S} S_d) \tag{4.6}$$

$\kappa_{g,J}, \kappa_{g,S}, \kappa_{d,J}, \kappa_{d,S}$ are the mean opacities for each source function. They are Planck mean opacity depending on the efficiency of line absorption and scattering. In most conditions, dust is in radiative equilibrium. The energy change within a dust grain is negligible.

(4) zeroth momentum of radiation field (radiative energy conservation)

$$\frac{1}{c}\frac{\partial}{\partial t} J + \frac{1}{c}\nabla \cdot (Jv) = -\nabla \cdot H - \frac{1}{c} K \nabla \cdot v + \frac{u}{c}\frac{3K - J}{r} - \rho(\kappa_{g,J} J - \kappa_{g,S} S_g + \kappa_{d,J} - \kappa_{d,S} S_d) \tag{4.7}$$

(5) first momentum of radiation field (radiative momentum conservation)

$$\frac{1}{c}\frac{\partial}{\partial t}H + \frac{1}{c}\nabla\cdot(Hv) = -\nabla K - \frac{3K-J}{r} + \frac{1}{c}H\nabla v - (\kappa_g + \kappa_d)\rho H \tag{4.8}$$

Equations 4.7 and 4.8 can be solved to get the radiation field intensity J and flux H. J, H, K are the zeroth, first and second moments of the radiation field,

$$J = \int I d\Omega \tag{4.9}$$

$$H = \int I cos(\theta) d\Omega \tag{4.10}$$

$$K = \int I cos^2(\theta) d\Omega \tag{4.11}$$

I is the field intensity from a specific direction. θ is the direction of the line of sight. κ_g can be obtained from studies of opacity in gas (Alexander & Ferguson, 1994; Ferguson et al., 2005). κ_{dust} is related to the dust formation and will be discussed next.

4.3 Dust formation

The effort of modeling dust mainly goes into two groups. (1) The brute force numerical solution of the master equation. this traces the full particle size spectrum and all possible reactions. It is widely used to calculated grain formation of small particles, e.g. how the nucleation starts from supersaturated vapor (Yamamoto & Nishida, 1977; Chesnokov & Krasnoperov, 2007). But it is not practical for very large grains as expected in cool star atmospheres. (2) The dust moment method developed by Gail et al. (1984); Gail & Sedlmayr (1985, 1987, 1988). This method considers that when the grain is large enough, the surface of the grain is relatively flat. So the addition of any molecules to the grain results in linear increase in the grain energy. This is of course only suitable for macroscopic grains and fit for the purpose of the dust calculation in cool star mass outflows. Macroscopic grains are such that the energy change is constant when adding an additional monomer into the grain.

The moments with respect to the size spectrum $f(N,t)$ of dust grains (N is the number of monomers in the dust grain, t is the time):

$$\mathcal{K}_i(t) = \int_{N_*}^{\infty} dN N^{i/3} f(N,t) \tag{4.12}$$

$\mathcal{K}_i(t)$ is the ith moment of the dust. A number of quantities about the dust can be derived from the moments.

a) number density of grains in the gas, N_{grain}:

$$N_{grain} = \int_{N_*}^{\infty} dN f(N,t) = \mathcal{K}_0. \tag{4.13}$$

b) number of density of monomers condensed into the grains, n_{mono},

$$n_{mono} = \int_{N_*}^{\infty} dN N f(N,t) = \mathcal{K}_3. \tag{4.14}$$

c) average number of monomers in a grain,

$$< N >= \mathcal{K}_3/\mathcal{K}_0. \tag{4.15}$$

d) average surface area,

$$< A >= 4\pi r_0^2 \mathcal{K}_2/\mathcal{K}_0. \tag{4.16}$$

r_0 is the radius of a monomer,

$$r_0 = (3W_{atom} m_p/4\pi\rho_{grain})^{1/3}. \tag{4.17}$$

e) average radius,

$$< r_{grain} >= \mathcal{K}_3/\mathcal{K}_0. \tag{4.18}$$

The dust moments in the Eulerian gird,

$$\frac{\partial \mathcal{K}_0}{\partial t} + \nabla \cdot (\mathcal{K}_0 v_d) = \mathcal{J}_d \tag{4.19}$$

$$\frac{\partial \mathcal{K}_i}{\partial t} + \nabla \cdot (\mathcal{K}_i v_d) = \frac{j}{d}\frac{1}{\tau}\mathcal{K}_{i-1} + N_l^{i/d}\mathcal{J}_d \tag{4.20}$$

These two equations combined with the equations in Section 1 make a whole set of equations for 2 fluid radiative hydrodynamic modeling. $\mathcal{J}_d$ is the nucleation rate of the dust. τ is the time scale of dust formation. These two quantities are discussed in detail in Gauger et al. (1990).

Another group of moment equations deal with heterogeneous growth of dust grains have been developed by Dominik et al. (1993); Helling & Woitke (2006). This allows so called "dirty grains" with higher formation rates. This is another interesting direction of exploration.

Numerous researchers have shown instabilities in the outflow. Popular mechanisms, such as exterior κ back warming effect and instability in the dust grain formation, were all calculated using the equations above. Woitke (2006) has shown a 2-D simulation with unique behaviors beyond the capability of 1-D codes. Higher dimension simulations can provide more realistic results. I have recently been granted the access to 3-D code Flash. It is the state of art 3-D code from University of Chicago ASC flash center. I am planning to implement the above equations in Flash code and realize a 3-D simulation of the dusty outflow.

BIBLIOGRAPHY

Alexander, D. R., & Ferguson, J. W. 1994, ApJ, 437, 879

Arndt, T. U., Fleischer, A. J., & Sedlmayr, E. 1997, AAP, 327, 614

Balick, B., Frank, A., 2002, ARAA, 40, 439-486

Barthes, D. 1998, AAP, 333, 647

Baud, B., & Habing, H. J. 1983, AAP, 127, 73

Bloecker, T. 1995, AAP, 297, 727

Bond, H. E., 2000, ASP conference: Asymmetrical Planetary Nebulae II: From Origin to Microstructures, 199, 115B

Bowen, G. H. 1988, ApJ, 329, 299

Bowen, G. H., & Willson, L. A. 1991, ApJL, 375, L53

Chabrier, G., & Baraffe, I. 2000, ARAA, 38, 337

Chandrasekhar, S. 1934, MNRAS, 94, 444

Chesnokov, E., Kransoperov, L., 2007, THE JOURNAL OF CHEMICAL PHYSICS 126, 144504

Corradi, R. L. M., et al., 2004, AAP, 417, 637-646

Dominik, C., Sedlmayr, E., & Gail, H.-P. 1993, AAP, 277, 578

Dwek, E. 1998, ApJ, 501, 643

Dreyer, C., Hegmann, M., & Sedlmayr, E. 2011, AAP, 525, A135

Dupree, A. K. 1986, ARAA 24, 377

Ferrarotti, A. S., & Gail, H.-P. 2001, AAP, 371, 133

Ferrarotti, A. S., & Gail, H.-P. 2002, AAP, 382, 256

Fleischer, A. J., Gauger, A., & Sedlmayr, E. 1992, AAP, 266, 321

Fleischer, A. J., Gauger, A., & Sedlmayr, E. 1995, AAP, 297, 543

Ferguson, J. W., Alexander, D. R., Allard, F., Barman, T., Bodnarik, J. G., Hauschildt, P. H., Heffner-Wong, A., & Tamanai, A. 2005, ApJj, 623, 585

Gail, H.-P., Keller, R., & Sedlmayr, E. 1984, AAP, 133, 320

Gail, H.-P., & Sedlmayr, E. 1985, AAP, 148, 183

Gail, H. P., & Sedlmayr, E. 1987, AAP, 171, 197

Gail, H.-P., & Sedlmayr, E. 1988, AAP, 206, 153

Gail, H.-P., & Sedlmayr, E. 1999, AAP, 347, 594

Gauger, A., Sedlmayr, E., & Gail, H.-P. 1990, AAP, 235, 345

Gilman, R. C. 1969, ApJL, 155, L185

Gilman, R. C. 1972, ApJ, 178, 423

Harpaz, A., Rappaport, S., & Soker, N., 1997, ApJ, 487, 809-817

Helling, C., & Woitke, P. 2006, AAP, 455, 325

Herwig, F. 2005, ARAA, 43, 435

Hill, S. J., & Willson, L. A. 1979, ApJ, 229, 1029

Höfner, S. 2008, AAP, 491, L1

Höfner, S. 2009, Cosmic Dust - Near and Far , 414, 3

Hoefner, S., & Dorfi, E. A. 1997, AAP, 319, 648

Huggins, P. J., & Glassgold, A. E. 1982, AJ, 87, 1828

Iben, I., Jr. 1967, ARAA, 5, 571

Iben, I., Jr. 1976, ApJ, 208, 165

Iben, I., Jr., & Renzini, A. 1983, ARAA, 21, 271

Iben, I., Jr. 1984, ApJ, 277, 333

Jura, M. 1986, ApJ, 303, 327

Jura, M. 1987, ApJ, 313, 743

Knapp, G. R., & Morris, M. 1985, ApJ, 292, 640

Knapp, G. R., & Morris, M. 1986, ApJ, 303, 521

Knapp, G. R., Gunn, J. E., & Connolly, A. J. 1995, ApJ, 448, 195

Kroupa, P. 2002, Science, 295, 82

Kudritzki, R.-P., & Puls, J. 2000, ARAA, 38, 613

Kwok, S., Su, K. Y. L., 1998, AJ, 501, L117-L212

Lamers, H. J. G. L. M., & Cassinelli, I. P. 1996, From Stars to Galaxies: the Impact of Stellar Physics on Galaxy Evolution, 98, 162

Marigo, P., & Girardi, L. 2007, AAP, 469, 239

Mastodemos, N., Morris, M., 1996, ApJ, 468, 851-860

Mastrodemos, N., Morris, M., 1999, ApJ, 523, 357-380

Mauron, N., & Huggins, P. J., 1999, AAP, 349, 203-208

Mauron, N., & Huggins, P. J., 2000, AAP, 359, 707-715

Mauron, N., & Huggins, P. J., 2006, AAP, 452, 257-268

Monnier, J. D., Geballe, T. R., & Danchi, W. C. 1998, ApJ, 502, 833

Morris, M., et al., 2006, IAUS 234: Planetary Nebulae in our Galaxy and Beyond, eds. M. J. Barlow & R. H. Méndez, 469

Netzer, N., & Knapp, G. R. 1987, ApJ, 323, 734

Nieuwenhuijzen, H., & de Jager, C. 1990, AAP, 231, 134

Nuth, J. A., III, & Ferguson, F. T. 2006, ApJ, 649, 1178

Origlia, L., Ferraro, F. R., Fusi Pecci, F., & Rood, R. T. 2002, ApJ, 571, 458

Ostlie, D. A., Cox, A. N., & Cahn, J. H. 1982, Pulsations in Classical and Cataclysmic Variable Stars, 297

Ostlie, D. A., & Cox, A. N. 1986, ApJ, 311, 864

Ragland, S., et al., 2008, AAS, 211, 5723R

Reimers, D. 1975, Problems in stellar atmospheres and envelopes., 229

Reimers, D. 1977, AAP, 61, 217

Rowan-Robinson, M., & Harris, S. 1983, MNRAS, 202, 767

Rowan-Robinson, M., & Harris, S. 1983, MNRAS, 202, 797

Ritchmyer, R. D., & Morton, K. W. 1967, Interscience Tracts in Pure and Applied Mathematics, New York: Interscience, 1967, 2nd ed.

Terzian, Y., Hajian, A. R., 2000, ASP conference: Asymmetrical Planetary Nebulae II: From Origin to Microstructures, 199, 33t

Sahai, R., et al., 1998, ApJ, 493, 301-311

Simis, Y. J. W., Icke, V., & Dominik, C. 2001, AAP, 371, 205

Vassiliadis, E., & Wood, P. R. 1993, ApJ, 413, 641

Wachter, A., Schröder, K.-P., Winters, J. M., Arndt, T. U., & Sedlmayr, E. 2002, AAP, 384, 452

Willson, L. A. 2000, ARAA, 38, 573

Willson, L. A., & Hill, S. J. 1979, ApJ, 228, 854

Willson, L. A., Wang, Q., Bowen, G. H., 2011, in process

Woitke, P. 2006, AAP, 460, L9

Woitke, P. 2006, AAP, 452, 537

Wood, P. R. 1979, ApJ, 227, 220

Ya'Ari, A., & Tuchman, Y. 1996, ApJ, 456, 350

Yamamoto, T., & Nishida, S. 1977, Progress of Theoretical Physics, 57, 1939